MDPI

Article

Geochemistry of REE and Other Critical Elements in Deep-Sea Polymetallic Nodules from Interoceanmetal (IOM) Exploration Area in Eastern Part of Clarion–Clipperton Fracture Zone, NE Pacific

Atanas Hikov [1,*], Zlatka Milakovska [1], Irena Peytcheva [1], Valcana Stoyanova [2], Elitsa Stefanova [1], Tomasz Abramowski [2,3], Milen Kadiyski [4], Silvia Chavdarova [1], Milen Stavrev [1] and Dimitrina Dimitrova [1]

[1] Geological Institute, Bulgarian Academy of Sciences, 24 Acad. G. Bonchev Str., 1113 Sofia, Bulgaria; zlatkam@geology.bas.bg (Z.M.); impeytcheva@gmail.com (I.P.); stefanova_e@geology.bas.bg (E.S.); silvia.chavdarova@gmail.com (S.C.); milen_stavrev07@abv.bg (M.S.); didi@geology.bas.bg (D.D.)

[2] Interoceanmetal Joint Organization, 9 Cyryla I Metodego Str., 71-541 Szczecin, Poland; valcanastoyanova@gmail.com (V.S.); t.abramowski@am.szczecin.pl (T.A.)

[3] Faculty of Navigation, Maritime University of Szczecin, 1-2 Wały Chrobrego Str., 70-500 Szczecin, Poland

[4] Aurubis Bulgaria AD, 2070 Pirdop, Bulgaria; kadiyski@gmail.com

* Correspondence: ahikov@geology.bas.bg

Abstract: Deep-sea Fe-Mn polymetallic nodules formed nowadays at the deep-sea ocean floor were evaluated as promising critical raw materials (CRMs). Here, we report results of polymetallic nodules from the H22_NE block of the Interoceanmetal (IOM) exploration area in the eastern part of the Clarion–Clipperton Zone (CCZ), NE Pacific Ocean. The polymetallic nodules were studied with X-ray Diffraction, Raman spectroscopy, SEM-EDS, and LA-ICP-MS (bulk nodules and in situ nodule layers). Additionally, we combine geochemical data of polymetallic nodules with the previously reported data of pore waters and sediments from six stations. Our study aims to define the mineral composition and determine the content of CRMs in the polymetallic nodules and to assess the main factors controlling metal deposition and nodule enrichment in some CRMs. Mn content and the Mn/Fe ratio of the nodules classify them mostly as mixed hydrogenetic–diagenetic type. They are also enriched in Ni, Cu, Co, Zn, Mo, W, Li, Tl, and REE. The in situ REE patterns exhibit MREE and HREE enrichment and a variable Ce anomaly that argues for a changing oxic/suboxic environment and periodically changing of diagenetic and hydrogenetic nodule growth. The results of the joint study of the bottom sediments, pore waters, and polymetallic nodules show a complexity of processes that influence the formation of these deposits. The changing oxic and anoxic conditions are well documented in the chemistry of the nodule layers. Probably the most important controlling factors are sedimentation rate, bioturbation, adsorption, desorption, and oxidation. In addition, growth rates, water depth variations, electro-chemical speciation, phosphatization, and the structures of the Fe-Mn adsorbents are also considered. The polymetallic nodule deposits in the IOM contract area are estimated for future mining for Ni, Cu, Co, and Mn resources. They, however, contain additional metals of economic importance, such as REE and other trace elements (referred to as CRMs) that are potential by-products for metal mining. They can significantly increase the economic importance of exploited polymetallic nodules.

Keywords: deep-sea polymetallic nodules; geochemistry; rare earth elements; critical elements; Clarion–Clipperton fracture zone

1. Introduction

The increasing consumption of raw materials and their limited distribution has led the European Union to define many rare and trace elements as critical raw materials (CRMs) [1]. The forecasts predict an increase in consumption, which empahsizes the importance of these critical raw materials especially related to the transition to a carbon-neutral future [2]. One of the most perspective new raw materials are deep-sea metalliferous sediments and iron–manganese (Fe-Mn) polymetallic nodules and crusts formed nowadays at the ocean floor. These polymetallic nodules would be a potential source for important elements for the green transition, such as REE, especially heavy REEs, Y and Sc [3–6]. The Fe–Mn nodule bearing Clarion–Clipperton Zone (CCZ) in the NE Pacific and the Fe–Mn prime crust zone (PCZ) in the Central Pacific are the areas of greatest economic interest for nodules, crusts, and sediments [3,7]. With the improvement of mining and processing systems, the deposits of polymetallic nodules could be economically feasible for exploitation within favourable market prices [8–10]. On the other hand, research must be conducted and measures taken to preserve the deep-sea environment and minimize the harmful impact of mining activities.

The genetic classifications of polymetallic nodules from the CCZ include three main types: hydrogenetic (H), diagenetic (D), and mixed hydrogenetic–diagenetic (HD) [11–13]. Hydrogenetic nodules are smaller, with low Mn/Fe ratios, low Ni and Cu, and high Co content. The HD nodules are 4–8 cm in size, with Mn/Fe ratios of 3–5. The diagenetic nodules are larger, with high Mn/Fe ratios and enriched in Mn, Cu, and Ni. The main Mn minerals in diagenetic nodules are todorokire/birnessite, whereas in the hydrogenetic type, vernadite dominates [13].

Here, we report results from a study of polymetallic nodules from thirteen stations in block H22_NE of the Interoceanmetal (IOM) exploration area in the eastern part of the Clarion–Clipperton Zone (CCZ), NE Pacific. In addition, we combine geochemical data of polymetallic nodules with the previously reported data of pore waters and sediments from six stations [14–16]. Our study has two main goals: (1) to define the mineral composition and determine the content of CRMs in the polymetallic nodules; and (2) to assess the main factors controlling the metal deposition and Fe-Mn polymetallic nodule enrichment in some CRMs. Comparison of the bulk nodule geochemistry with in situ geochemical analyses in different mineral phases and layers allowed us to determine the main CRM-bearing phases that contribute to the elevated content of these elements in the nodules. In a broader perspective, the reported results allow for the estimation of the potential of polymetallic nodules as a source of critical elements. The survey of polymetallic nodule resources and bottom sediments contributes to a better understanding of a possible anticipated environmental impact during further exploration and technological extraction experiments.

2. Geological Setting and Sampling

The examined area is one of the most perspective parts of the IOM licence area for nodule exploitation, named the H22_NE exploitable block. It covers 630 km^2 of the seafloor in the eastern part of the Clarion–Clipperton fracture zone, NE Pacific Ocean, between 11°06′–11°26′ N latitude and 119°25′–119°42′ W longitude at depth from 4300 to 4500 m (Figure 1). The explored stations are distributed among various geomorphological types, represented mostly by undulating hilly plains, intersected by longitudinal ridges and depressions oriented in the meridional direction, and sub-parallel volcanic massifs [17,18]. All sampled stations are located below the critical carbonate compensation depth. The sediment profile is topped by slightly siliceous silty clay and siliceous silty clay (according to the Kotlinski, 2010, classification [18]). Sediments contain up to 28.6% amorphous silica and are characterized by reduced bulk density and increased moisture content. The sedimentation rate in the IOM area is between 0.2 and 1.15 cm/kyr [19,20].
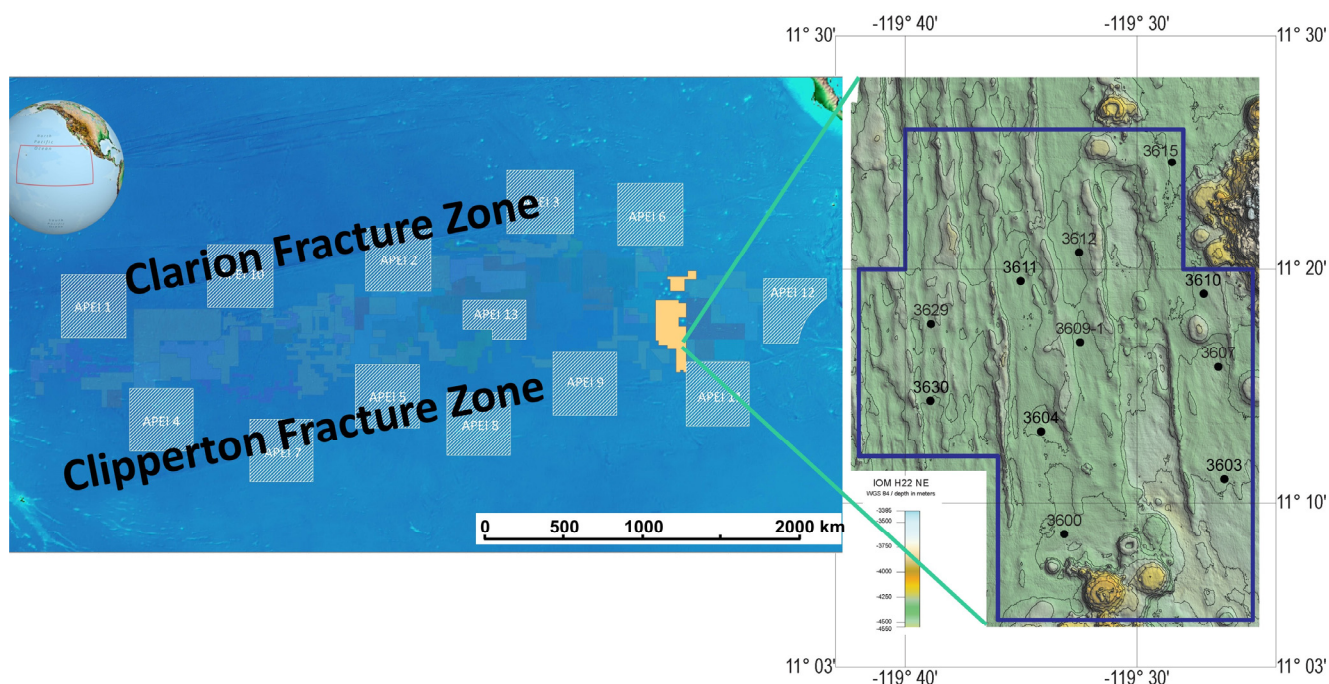
Figure 1. The location of the sampling area in the IOM exploration site (yellow) in the eastern part of the Clarion–Clipperton fracture zone (CCZ) (red rectangle), NE Pacific (left; adapted from [21]), and a geomorphological map of the seafloor of the IOM H22_NE exploitable block (right (blue box); adapted from [14,17]). The black dots with numbers indicate the tested sampling stations. The white boxes are Ares of Particular Environmental Interest (APEIs).

2.1. Sampling

Box-corer samples from the sampling stations were collected during the IOM'2019 expedition. Relatively undisturbed bottom samples from up to 50 cm in depth were yielded. After collecting the nodules from the surface, four sediment layers at depths of 0–3, 3–5, 5–10, and 10–20 cm were sampled. The sediment samples for pore water extraction were collected on board from the depth intervals of 0–5, 10–15, 25–30, and 35–40 cm following the recommendations of ISBA/19/LTC/8 [22]. Data on board processing of the sampled stations showed that wet nodule abundance parameter ranges from 10.3 to 19.9 kg/m^2, averaging 13.5 kg/m^2; whereas the nodule coverage calculated using spot photographs of the seabed varies from 18% to 50% with an average of 40% [14]. The sampling was performed on thirteen stations from the H22_NE exploitable block of the IOM licence area, whereas seventeen nodules were separated.

2.2. Sediment Composition

Sediment composition at all stations is dominated by light brown siliceous silty clays with irregular dark patches [14,23]. The top 7–12 cm layer includes semi-liquid, predominantly dark brown-coloured, siliceous silty clay, denoted as a geochemically active layer (GAL), the medium for polymetallic nodule formation. The redox potential (Eh) value of the GAL ranges from +462 mV to +545 mV and decreases with depth. The active reaction (pH) of the environment is mostly neutral, changing weakly from 7.01 to 7.52 [14,23].

The authors' results on the bulk sediment samples [14,23] indicated that the sediments are composed of fine silts according to the Krumbein scale [24]. They are predominantly poorly sorted with bimodal particle size distribution. The silt and sandy fractions show opposite trends of variation, whereas the clayey fraction quantity increases with depth. An amorphous phase predominates, representing biogenic opal-A, authigenic Fe-Mn (hydr)oxides, and clay minerals. This amorphous phase of biogenic opal-A (>30%)

defines the sediments as clayey siliceous ooze according to the classifications of Lisitzin [25] and Kotliński [18] or the modified classifications of Lisitzin [25] in Kotliński [18]. The crystalline phases illite, kaolinite, chlorite, quartz, and andesine represent a detrital component, while halite, cristobalite, and barite are of authigenic origin. Illite, illite/smectite, chlorite/vermiculite and kaolinite, and quartz admixture were detected in all fractions <2 μm [14,23].

The chemical composition of the sediment samples shows a high Al/(Al + Fe + Mn) ratio (0.57) and could be considered as non-metalliferous [26], although they host significant amounts of Fe-Mn nodules. Manganese, Mn/Fe ratio, Co, Ni, Cu, and Ba have the highest contents in the GAL that decrease with depth, Fe content has the opposite behaviour, while REE do not show any significant variations between the sediment layers. PAAS-normalized REE patterns show MREE and HREE enrichment and negative Ce anomalies [14].

2.3. Pore Water Composition

Pore water composition was studied by [15,16]. Most of the station samples have maximum values of Fe, Mn, Ni, Cu, and Co in the second (10–15 cm) or the first (0–5 cm) layers. The ΣREE in the pore water samples also have maximum values in the first or the second layers. A negative Ce anomaly predominates and increases with depth [15,16].

3. Methods

The nodule morphology, size, and surface texture were described macroscopically. The mineral composition of the polymetallic nodules was studied in polished sections by standard petrography, combined with X-ray Diffraction (XRD; Malvern Panalytical Multipurpose X-ray Diffractometer Empyrean at the Institute of Physical Chemistry, Bulgarian Academy of Sciences) and Raman spectroscopy. The Raman spectra were obtained using the LabRAM HR Visible Raman spectrometer (HORIBA, Jobin Yvon) at the Faculty of Physics, Sofia University. For excitation, the 633 nm line of a He-Ne laser was used, the diameter of the illuminated spot on the sample surface was about 3 μm, the investigated spectral range was 90 cm^{-1}–1280 cm^{-1}, and the wavenumber accuracy was 1 cm^{-1}. Mineral phase diversity, internal structure, and major element composition of the nodules were determined by SEM-EDS (SEM JEOL JSM-6610LV at the University of Belgrade, Serbia; X-MaxN 50 EDS detector by Oxford Instruments, installed on a TESCAN VEGA 3 XMU scanning electron microscope (20 kV accelerating voltage) at the Research and Development Department of Aurubis Bulgaria AD, Pirdop). The chemical composition of bulk nodule samples was measured on pressed pellets by the LA-ICP-MS method (New Wave UP193FX excimer laser combined with a PerkinElmer ELAN DRC-e ICP-MS) at the Geological Institute, Bulgarian Academy of Sciences (BAS). In situ LA-ICP-MS analyses were also performed in different nodule layers on a polished section to determine the trace element content. We measured 66 elements in total: Li^7, Be^9, B^{11}, Na^{23}, Mg^{25}, Al^{27}, Si^{29}, P^{31}, S^{32}, K^{39}, Ca^{42}, Sc^{45}, Ti^{49}, V^{51}, Cr^{53}, Mn^{55}, Fe^{57}, Co^{59}, Ni^{60}, Cu^{65}, Zn^{66}, Ga^{71}, Ge^{74}, As^{75}, Se^{77}, Rb^{85}, Sr^{88}, Y^{89}, Zr^{90}, Nb^{93}, Mo^{95}, Pd^{105}, Ag^{107}, Cd^{111}, In^{115}, Sn^{118}, Sb^{121}, Te^{125}, Cs^{133}, Ba^{137}, La^{139}, Ce^{140}, Pr^{141}, Nd^{146}, Sm^{147}, Eu^{151}, Gd^{157}, Tb^{159}, Dy^{163}, Ho^{165}, Er^{167}, Tm^{169}, Yb^{173}, Lu^{175}, Hf^{178}, Ta^{181}, W^{182}, Re^{185}, Pt^{195}, Au^{197}, Hg^{202}, Tl^{205}, Pb^{208}, Bi^{209}, Th^{232}, and U^{238}. The laser spot was 35 μm and 6 Hz pulse rate for in situ mineral analyses, and 50 μm and 6 Hz for bulk nodule samples. On pressed pellets, at least three measurements were taken per sample. NIST SRM 610 glass and Mass1 polymetallic standards were used as external standards. The total major element oxides (100 wt. %) was used as a standardization method for the pressed pellets after subtracting the loss of ignition (LOI). For the in situ trace element composition, the manganese contents from SEM-EDS analyses were used as

an internal standard for transforming the element intensity during analyses into absolute concentrations. Data reduction was conducted using SILLS ver. 1.1.0 software [27].

4. Results

4.1. Morphology and Mineralogy of Nodules

The studied polymetallic nodules (the numbers mean sample stations) have botryoidal, ellipsoidal, discoidal, spheroidal, or irregular shapes (Figure 2a–d). Generally, the small nodules up to 3 cm (Figure 2f,h) in diameter have spheroidal or discoidal compact morphology. The larger nodules (5–10 cm in diameter) usually have an asymmetrical shape with complex morphology. The surface texture of the nodules is smooth or granular. Traces of benthic organism activity are more visible on the smooth surface of small hydrogenitic [13] nodules (Figure 2h). Pores on the surface or inside the nodules are filled with sediment material and radiolarian tests. The nodule nuclei are presented by lithified sediment fragments (mainly hydrogenitic [19] nodules) or bioclastics and older nodules (mainly diagenitic [19] nodules) (Figure 3c,d,f). The large nodules have complex nuclei, probably of older nodule fragments. The cross sections of nodules (Figure 2g) reveal one or more "core" zones (older nodules as the nucleus) especially the large ones. Nodule 3623-p has a compact massive rectangular old nodule as core zone (Figure 3h). Nodule 3607 has the largest amount of sediment filling material (Figures 2e and 3b). The small nodules show distinct zoning represented by varying colour and thickness bands of concentric ore-bearing microlayers.

The polymetallic nodules have complex phase composition. They consist of a mixture of different materials, such as organic and colloidal matter, with fragments of mineral and biogenic origin. The mineral fragments (crystallites) can be detrital or authigenic. The mineral phases in nodules are micro- to fine-grained, poorly crystalized, and intimately intergrown. Most of them are amorphous and cannot be determined by X-ray Diffraction. Electron microprobe analysis can only show chemical composition, which cannot give insights into whether this phase is crystal or amorphous.

XRD spectra of the studied nodules are very similar (Figure 4). The crystalline mineral phases identified with certainty are 10 Å manganate (todorokite) and quartz. The identification of muscovite and vernadite is not very clear because of the overlap of their peaks and the small quantities of these phases. Muscovite dominates only in nodule 3607, which contains the largest amount of sediment filling. Todorokite is amounts from 70% to 86.9% of the crystalline phases. The amorphous phases dominate over crystalline phases. A semi-quantitative assessment shows that the amorphous phases build from 89 to 91% of the nodules. Most likely, the main part of manganese forms poorly crystalline and amorphous phases. The presence of todorokite in the nodules was also confirmed by Raman spectroscopy (Figure 5).
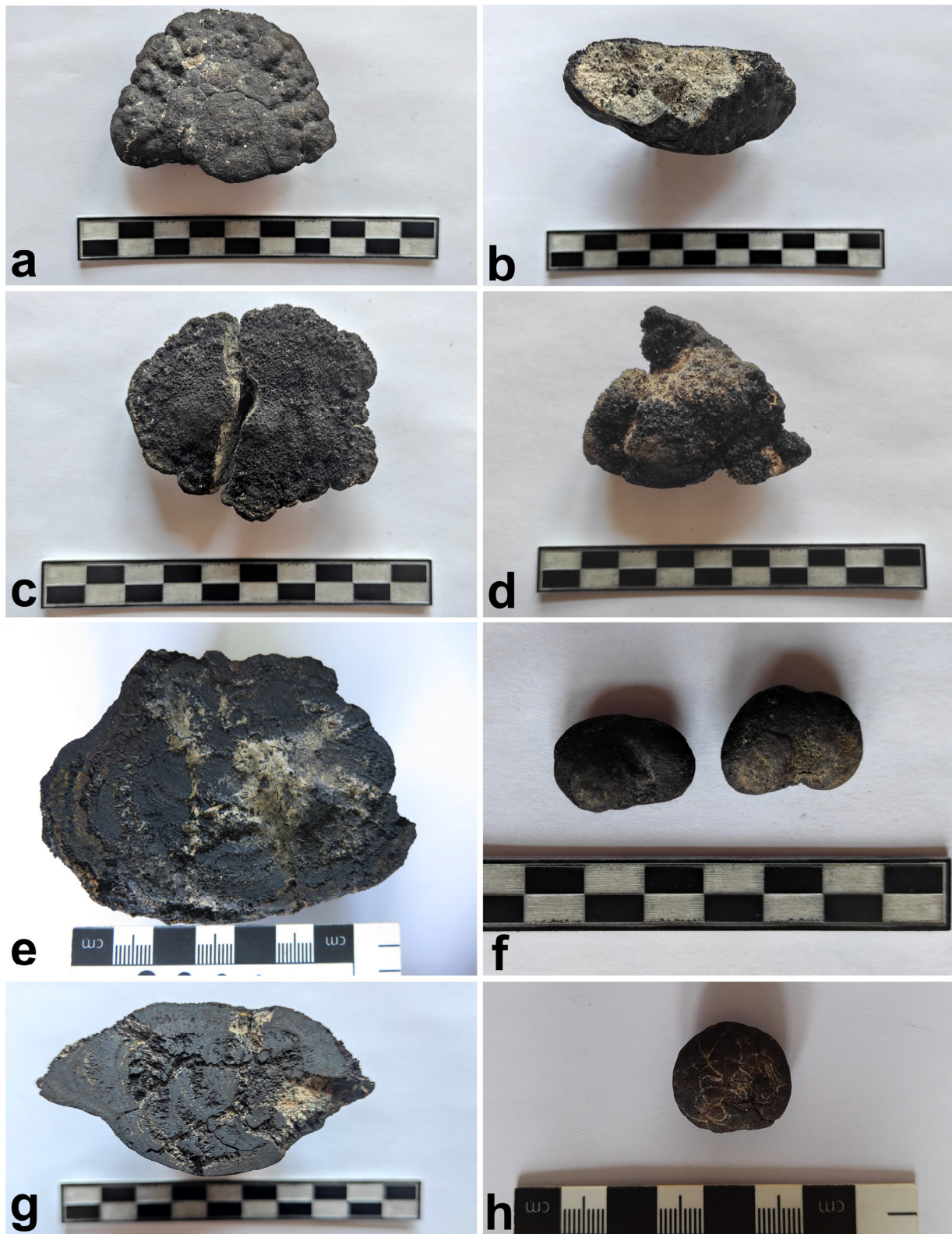
Figure 2. Examples of polymetallic nodules: (**a**) 3603; (**b**) 3610-1; (**c**) 3604; (**d**) 3611; (**e**) 3607; (**f**) 3623-p; (**g**) 3630; (**h**) 3615. Numbers are sample stations.
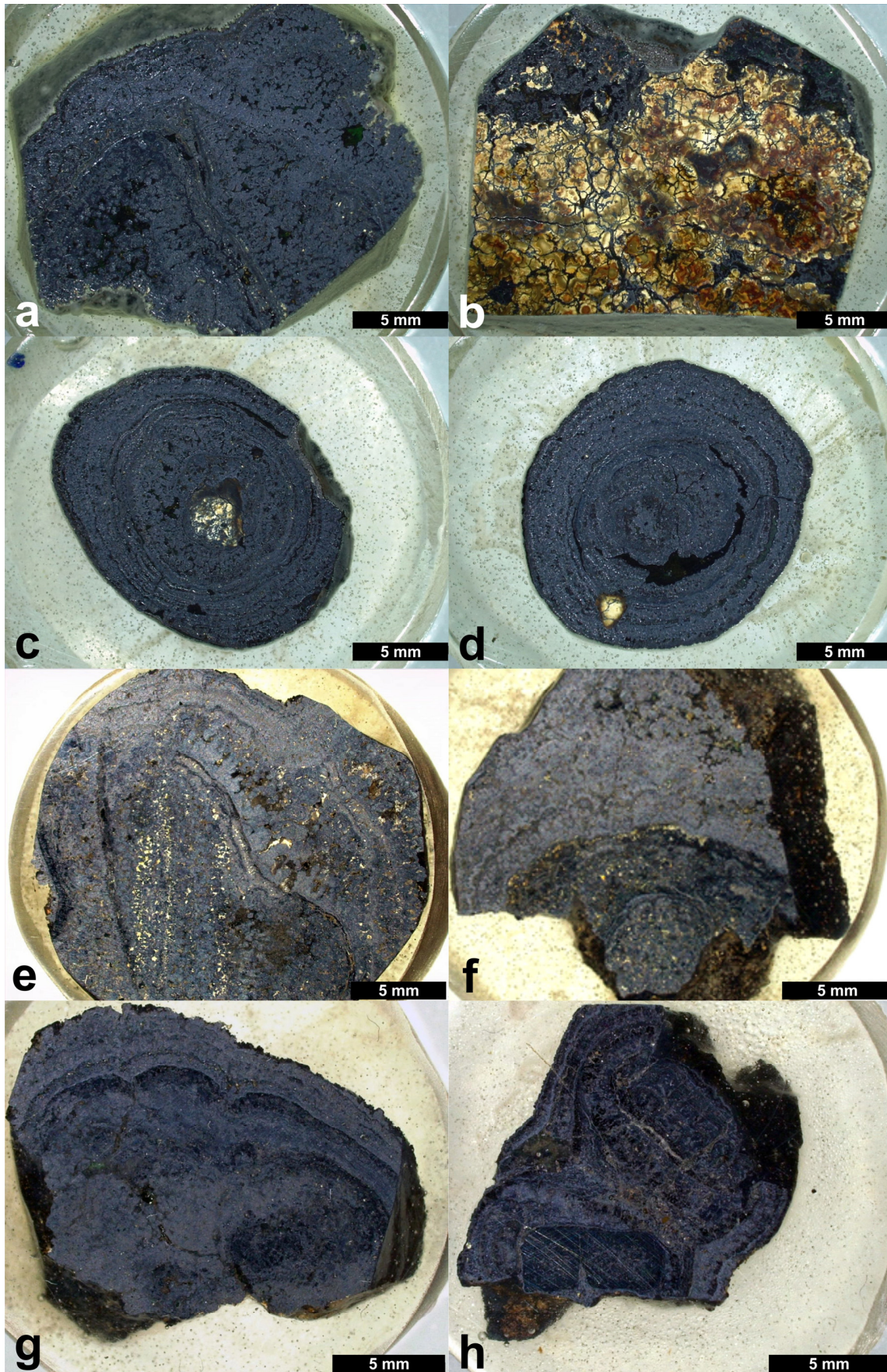
Figure 3. Examples of polished sections of polymetallic nodules: (**a**) 3600; (**b**) 3607; (**c**) 3609-1; (**d**) 3612; (**e**) 3611; (**f**) 3630; (**g**) 3621; (**h**) 3623-p. Numbers are sample stations.
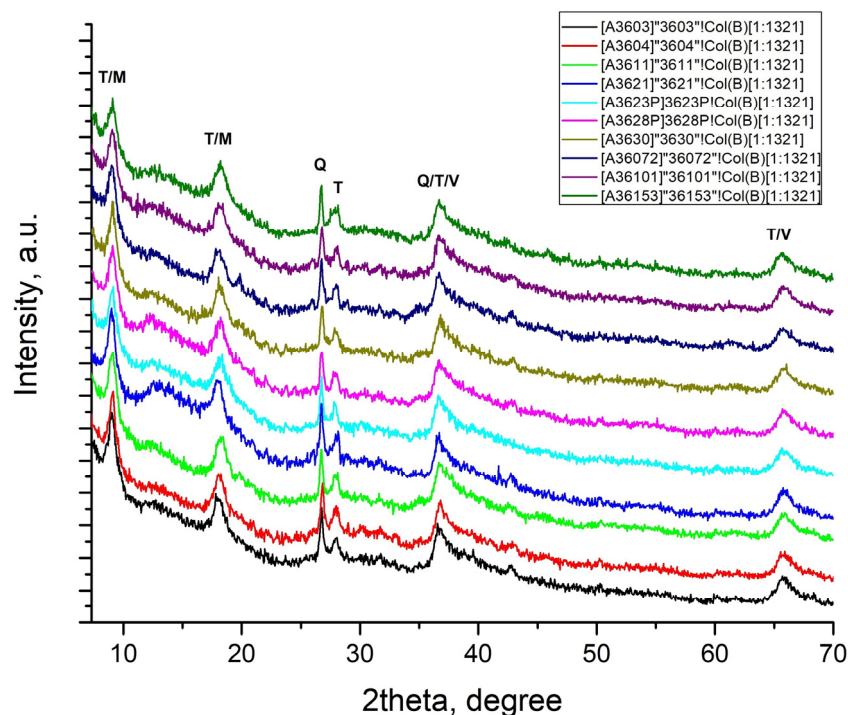
Figure 4. XRD spectra of studied nodules (T—todorokite; M—muscovite; Q—quartz; V—vernadite).
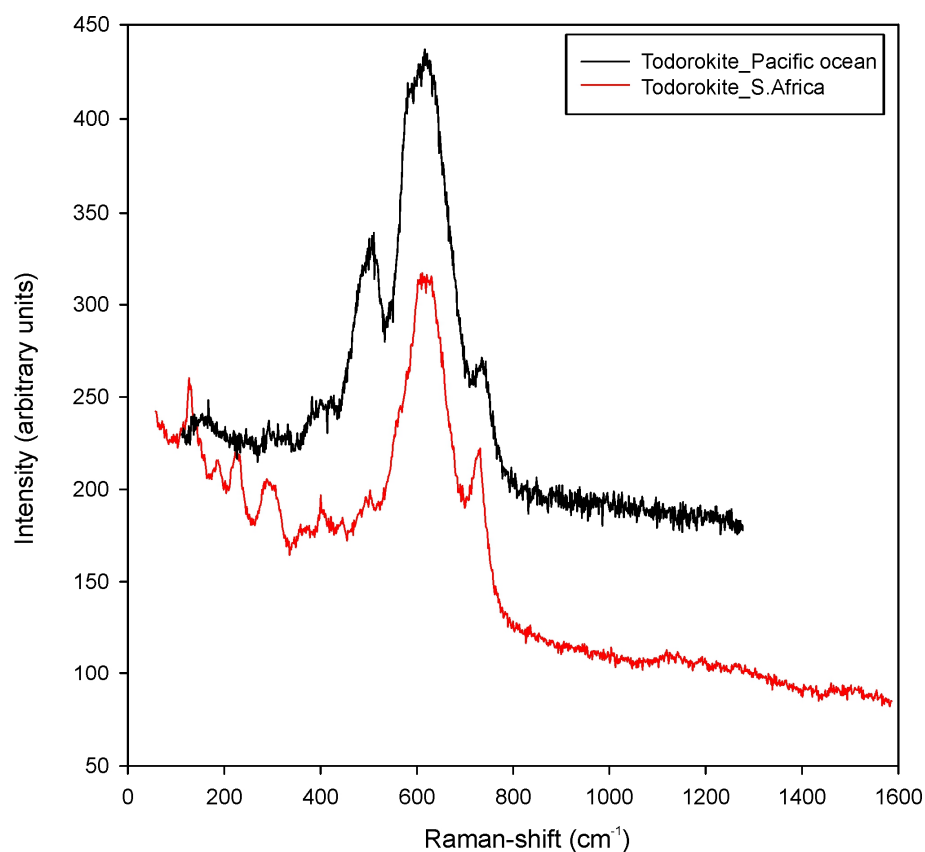

Figure 5. Raman spectra of todorokite from CCZ compared to todorokite from South Africa [28].

4.2. Geochemistry of Nodules

4.2.1. Geochemistry of Bulk Nodules

The modern deep-sea polymetallic nodules contain a significant quantity (about 1/3rd of the nodule's weight) of free/pore water and crystalline water [17,29]. We measured free

water from 6.26% to 14.01% after heating to 105 °C and LOI (loss of ignition) from 15.60% to 19.72% after heating to 1050 °C. Total loss varies from 22.10% (3607) to 33.04% (3604), and the mean is 26.45%.

The results of the LA-ICP-MS analyses of bulk nodule samples (Table S1) show Mn contents from 22.62 to 35.59%, with a mean of 30.61%, and Fe from 3.47 to 8.26%, with a mean of 5.58%. The Mn/Fe ratio is from 2.74 to 10.12, with a mean of 6.04. The concentrations of main oxides are as follows: SiO_2 (9.23–23.88, mean of 12.95 wt. %), Al_2O_3 (3.23–5.45, mean of 3.77 wt. %), TiO_2 (0.19–0.45, mean of 0.33 wt. %), MgO (2.03–3.06, mean of 2.64 wt. %), CaO (1.31–2.29, mean of 1.96 wt. %), Na_2O (2.80–4.03, mean of 3.39 wt. %), K_2O (1.12–2.10, mean of 1.46 wt. %), and P_2O_5 (0.27–0.49, mean of 0.37 wt. %).

The nodules contain significant contents of characteristic elements such as Ni, Cu, Co, Zn, Mo, W, Li, Tl, Pb, and REE. High contents of V, As, Sr, Y, Cd, Sb, and Ba are also detected (Table 1).

Table 1. The LA-ICP-MS bulk nodule data for 17 polymetallic nodules from the H22_NE block of the IOM exploration area in the eastern part of the CCZ, NE Pacific.

	Min	**Max**	**Mean**		**Min**	**Max**	**Mean**
Mn, %	22.62	35.59	30.61	Ba, ppm	2197.00	5775.00	3526.00
Fe	3.47	8.26	5.58	La	48.53	120.65	79.56
Cu	1.07	1.50	1.26	Ce	119.66	307.12	200.70
Ni	0.58	1.70	1.29	Pr	14.10	37.04	23.78
Co	0.12	0.30	0.21	Nd	59.23	150.11	97.52
Zn	0.09	0.26	0.18	Sm	14.76	33.39	23.17
Li, ppm	77.00	205.00	142.50	Eu	3.49	8.25	5.76
Sc	5.26	12.87	8.48	Gd	12.99	31.06	21.13
V	381.00	595.00	473.00	Tb	2.05	4.63	3.23
Ga	26.40	51.6.	39.10	Dy	11.71	27.05	18.58
As	67.00	158.00	108.00	Ho	2.18	5.17	3.49
Sr	431.00	656.00	567.00	Er	6.13	14.32	9.74
Y	41.00	83.00	61.00	Tm	0.83	1.98	1.38
Zr	110.00	340.00	218.00	Yb	5.97	12.73	9.27
Mo	430.00	872.00	737.00	Lu	0.80	2.02	1.34
Pd	0.34	1.53	0.88	W	55.00	111.00	72.00
Cd	8.61	24.22	18.23	Tl	53.00	410.00	226.00
Sn	0.63	9.52	5.21	Pb	247.00	616.00	397.00
Sb	35.00	67.5	53.60	Bi	2.22	7.07	4.40
Te	2.75	10.29	5.65	Th	4.72	14.54	9.10
Cs	1.91	187.5	20.7	U	2.61	4.58	3.53

The ΣREE varies from 307.27 to 719.11 ppm (mean: 498.64 ppm), ΣREY is from 348.03 to 800.78 ppm (mean: 559.71 ppm), and ΣHREE is from 47.00 to 105.48 ppm (mean: 73.91 ppm). Chondrite-normalized REE patterns (Figure 6a) of all bulk nodule samples are similar with LREE enrichment and comparatively flat MREE and HREE patterns. All patterns have positive or slight negative Ce (Ce/Ce* = 0.93–1.30) and negative Eu (Eu/Eu* = 0.72–0.84) anomalies. PAAS-normalized REE patterns (Figure 6b) show enrichment of all REE, especially of MREE and HREE. Most of the patterns have a positive or

slight negative Ce (Ce/Ce* = 0.89–1.24) anomaly, and positive Eu (Eu/Eu* = 1.13–1.30) and negative Y (Y/Y* = 0.55–0.68) anomalies.
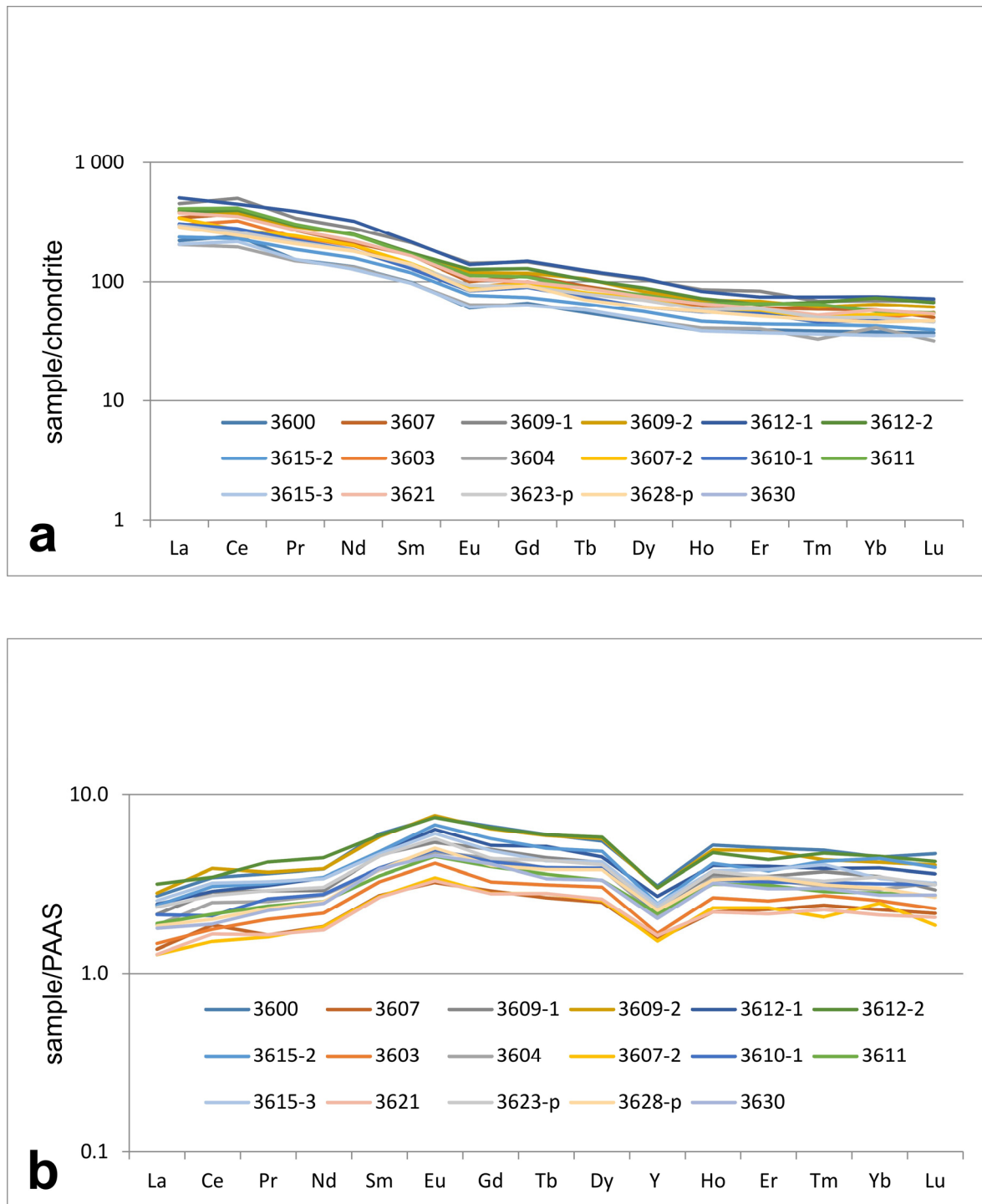

Figure 6. (**a**) Chondrite-normalized (after [30]) and (**b**) PAAS-normalized (after [31]) REE patterns of bulk nodule samples. Numbers are sample stations.

4.2.2. SEM Analyses of Nodules

The internal structure of the nodules was studied on polished sections by optical reflected light microscopy and scanning electron microscopy (SEM). The zonal pattern of each nodule, especially large ones, is unique. Distinct zoning from core to edge is observed mostly in small nodules. In Figure 7, zoning of the nodules is represented by continuous, varied bands. Some of the bands have thin uniform layers, whereas

other bands are formed by layers of dendritic oxyhydroxides. Each band represents thin layers, sometimes 1–2 microns wide (Figure 7), of manganese oxyhydroxides with different manganese content. The nodule cores and interstices between manganese oxyhydroxide dendrites are filled with detrital sediment material such as clay minerals, chlorite, Na-K micas, and quartz, as well as apatite and barite with authigenic origin (Figure 8). Barite forms single crystals or very fine grains, which are deposited between colloform layers of Fe-Mn oxyhydroxides (Figure 8e). Sometimes, manganese oxyhydroxides fill cracks in the sediments and form thin veinlets (Figure 8b).
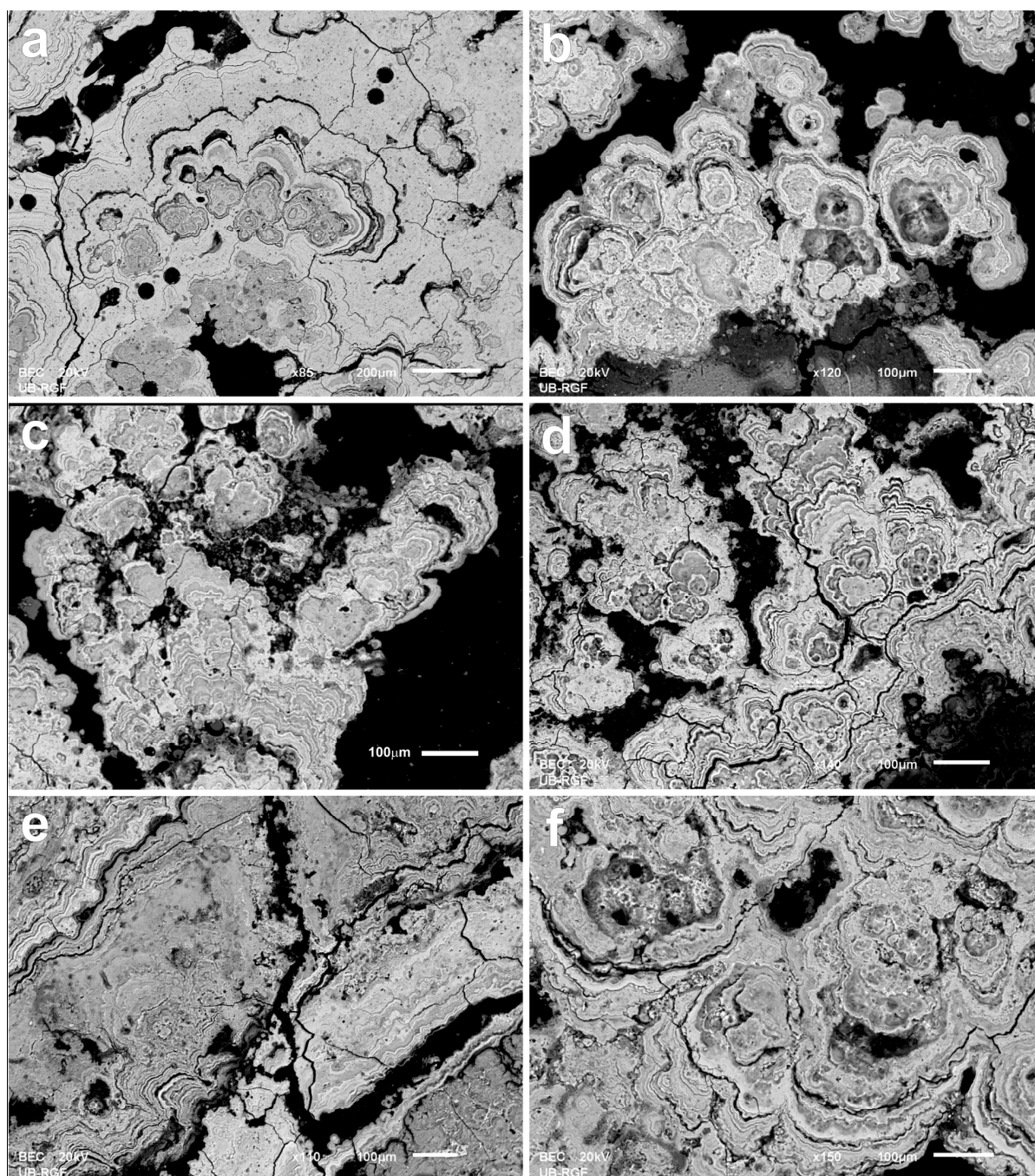

Figure 7. SEM-BSE images representing fine colloform textures of polymetallic nodules: (**a**) 3600; (**b**) 3607; (**c**) 3609; (**d**) and (**e**) 3515; (**f**) 3612. Numbers are sample stations.
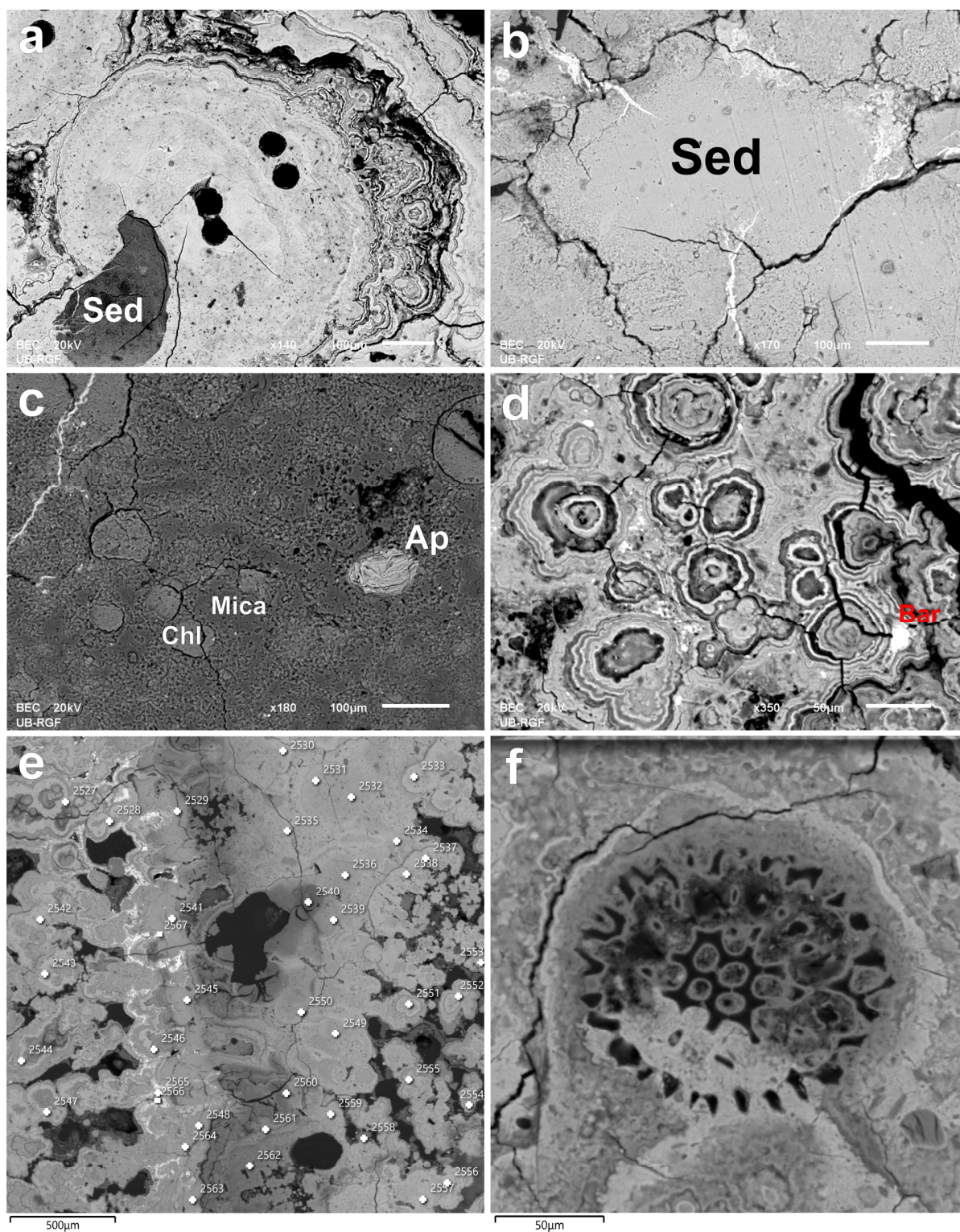
Figure 8. SEM-BSE images representing detrital and authigenic mineral phases of polymetallic nodules: (**a**) 3600; (**b**) 3607; (**c**) 3612; (**d**) 3615 (Sed—sediment; Chl—clorite; Mica—Na-K mica; Ap—apatite; Bar—barite); (**e**) fine barite crystals (white) deposited between colloform layers of Fe-Mn oxyhydroxides and dehydration cracks in grey bands (3611); (**f**) radiolarian skeleton partly replaced by Mn oxyhydroxide mineral phase (3621). Numbers are sample stations.

The light-grey bands and layers are rich in manganese, whereas the dark bands are poor in manganese. Some dark bands are sometimes rich in iron, and some dark-grey bands are poor in iron. Most likey, the grey bands are composed of amorphous or poorly

crystalline mineral(s) with very high water content confirmed by low total sum of elements of SEM analyses. The statement could be additionally confirmed by the dehydration cracks usually formed when the nodules were separated from the sediment on board. Sometimes, radiolarian tests partly or completely replaced by manganese oxyhydroxides were observed in the nodules (Figure 8f).

EDS mapping confirms the Mn enrichment in lighter bands and layers (Figure 9). The distribution of oxygen is overlapping the Mn one, which means manganese is in high valent state, with Mn^{4+} and Mn^{3+} incorporated in todorokite/birnesite. Similar distribution is observed in Ni, Cu, partly Na, and Zn. Si, Al, Ca, and Na content increases only in tiny layers probably with detrital mineral phases. Iron is high in some dark bands and only Cl increases in places where iron decreases.

The SEM-EDS analyses reveal the variable composition of nodule layers. The results allow a distinction of at least four groups of Fe-Mn oxyhydroxide phases.

(1) Phases with a Mn content >40%, Fe from 0% to 5.6%, and Mn/Fe ratios between 10 and 143. These phases are enriched in Cu (0.93%–3.51%) and Ni (0.71%–3.37%). Typical impurities are Mg (0.75%–6.43%), Na (0.68%–3.27%), K (0.24%–2.71%), Ca (0.78%–2.34%), Al (0.26%–3.51%), and Si (0.10%–6.37%). A sporadic presence is detected for P, Co, Ti, Cl, S, Zn, and Ba. These Mn-rich phases have chemical compositions that correspond to todorokite/birnessite.

(2) Phases with a Mn content of 30%–40%, Fe of 0.59%–6.11%, and Mn/Fe ratios of 5.62–63. They also have increased contents of Cu (0.63%–2.37%) and Ni (0.39%–3.03%). Some analyses show a high content of Co (0.26–1.00%). Common major elements are Mg (1.14%–4.89%), Na (0.38%–2.05%), K (0.42%–1.20%), Ca (0.65%–4.33%), Al (0.30%–4.94%), and Si (0.15%–6.56%); some of them are slightly higher than in the first group. These are mixed Mn-rich phases probably of lower crystallinity compared to the first group.

(3) Phases with a Mn content from 15.41% to 37.70% and a considerable Fe content (3.96%–24.12%). These phases have very low Mn/Fe ratios (0.62–6.86), Ni (0%–1.50%), and Cu (0%–1.31%). High concentrations are detected for Si (1.34%–13.94%) and P (0.08%–0.49%) while Al (0.42%–3.47%), Mg (0.61%–3.62%), and Ca (0.63%–2.57%) have low concentrations. These phases probably correspond to the mineral vernadite.

(4) Phases with low (<50 wt. %) total analytical sum. They are usually found in the dark layers. Manganese dominates, and some analyses show high Fe content, with Ni and Co also present. The group probably contains amorphous Fe-Mn oxyhyrdoxide phases with high water content and cannot be unambiguously identified. These manganese phases could also be interpreted as birnessite-like structures containing interlayer water [32].

4.2.3. In Situ LA-ICP-MS Analyses of Nodules

The in situ LA-ICP-MS analyses (Table S2) confirm the significant variations in element concentrations between nodule layers detected by SEM-EDS. Manganese content varies from 10.75 to 57.63 (mean: 35.28%) and Fe from 0.10 to 24.12 (mean: 4.89%). The Mn/Fe ratio is from 0.01 to 491.75 (mean: 26.54). There are high contents of Ni (0.13–3.58, mean 1.43%) and Cu (0.20–3.21, mean: 1.40%). Other elements are as follows: Co (0.005%–1.04%), Zn (0.027%–0.85%), Ba (0.04%–2.64%), Mo (195–2114 ppm), W (23–607 ppm), Li (15.5–1046 ppm), Tl (26–1101 ppm), Pb (24–2917 ppm), Sc (0.93–35.5 ppm), V (161–2542 ppm), As (21–402 ppm), Sr (122–1539 ppm), Y (14.76–196.6 ppm), Zr (25–1301 ppm), Cd (1.43–54.1 ppm), Sb (10–189 ppm), Bi (0.07–34.6 ppm), Th (0.48–49.6 ppm), and U (0.5–13.1 ppm). The ΣREE varies from 119.3 to 2312 (mean: 622.24) ppm, ΣREY varies from 134.05 to 2509 (mean: 690.75) ppm, and ΣHREE varies from 32.99 to 470.25 (mean: 158.39) ppm. Although large variations in elements between layers are observed, there are no trends of increase or decrease in element concentrations from cores (nuclei) to

the outer zones of the nodules. The behaviour of the trace elements depends mainly on the distribution patterns of Mn and Fe, and to a degree of Ti, P, Ca, and Ba.
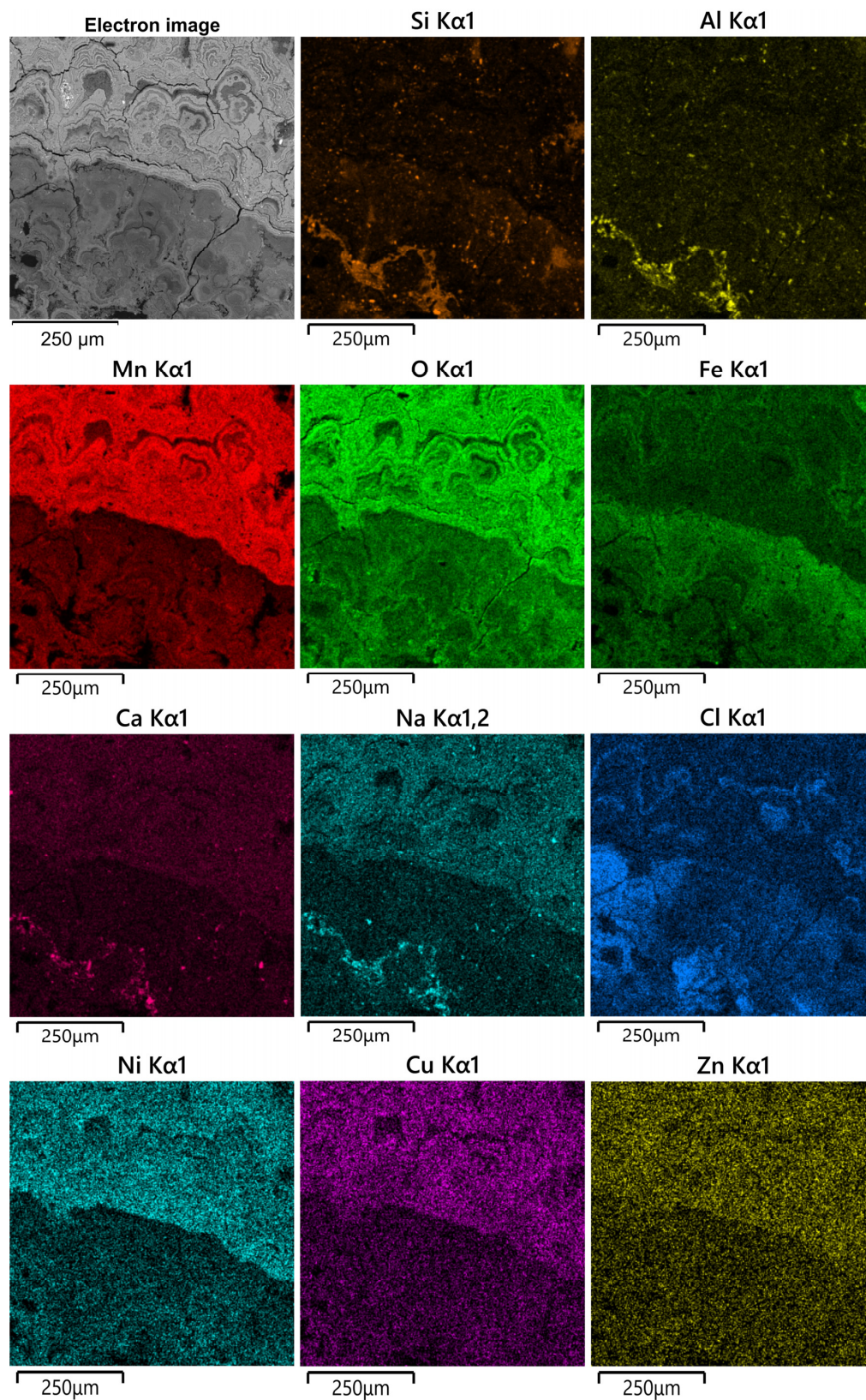
Figure 9. BSE image and EDS maps for distribution of Si, Al, Mn, O, Fe, Ca, Na, Cl, Ni, Cu, and Zn of part of sample 3611.

The chondrite-normalized REE patterns (Figure 10a) of the in situ nodule analyses confirm the LREE enrichment and comparatively flat MREE and HREE patterns revealed by the bulk nodule analyses. A main difference found is in the Ce anomaly: half of the layers have negative Ce anomalies, whereas the other half have positive Ce anomalies (Ce/Ce* = 0.14–3.43). Most of the patterns have a negative Eu anomaly, and some have a slightly positive Eu anomaly (Eu/Eu* = 0.26–1.20). The PAAS-normalized REE patterns (Figure 10b; 11) show MREE and HREE enrichment. Approximately half of the patterns have a negative Ce anomaly, and the rest have a positive Ce anomaly (Ce/Ce* = 0.13–3.23). Most analyses show a weak positive Eu (Eu/Eu* = 0.40–1.84) anomaly and all have a negative Y (Y/Y* = 0.36–0.79) anomaly. All in situ analyses of nodule 3607 have a positive Ce anomaly (Figure 11) that corresponds to a low Mn/Fe ratio and low Ni and Cu contents in this nodule. Ce anomaly has a weak negative correlation (−0.46) with the Mn/Fe ratio for all in situ nodule analyses.
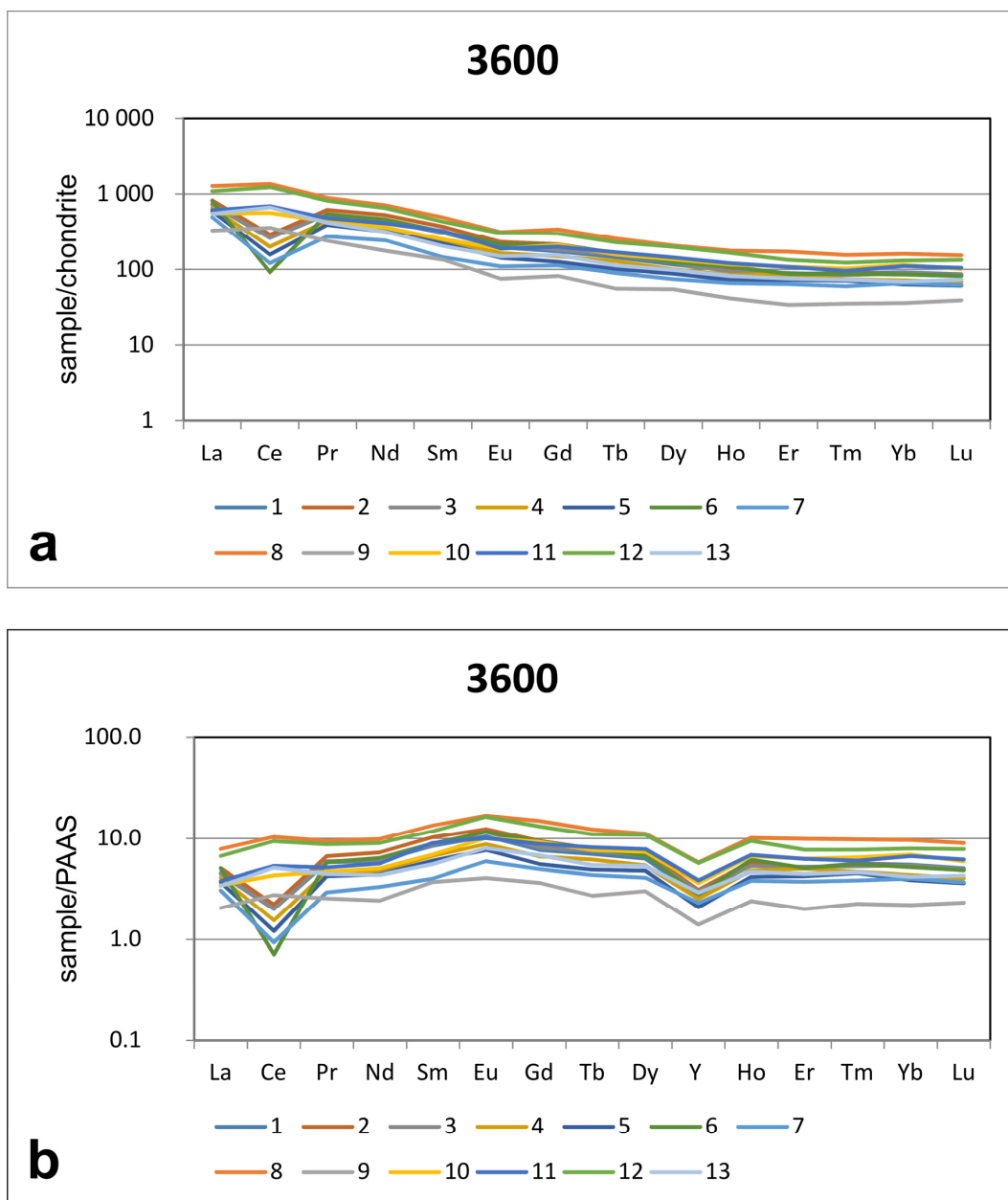

Figure 10. (**a**) Chondrite-normalized (after [30]) and (**b**) PAAS-normalized (after [31]) REE patterns of in situ analyses of nodule 3600.
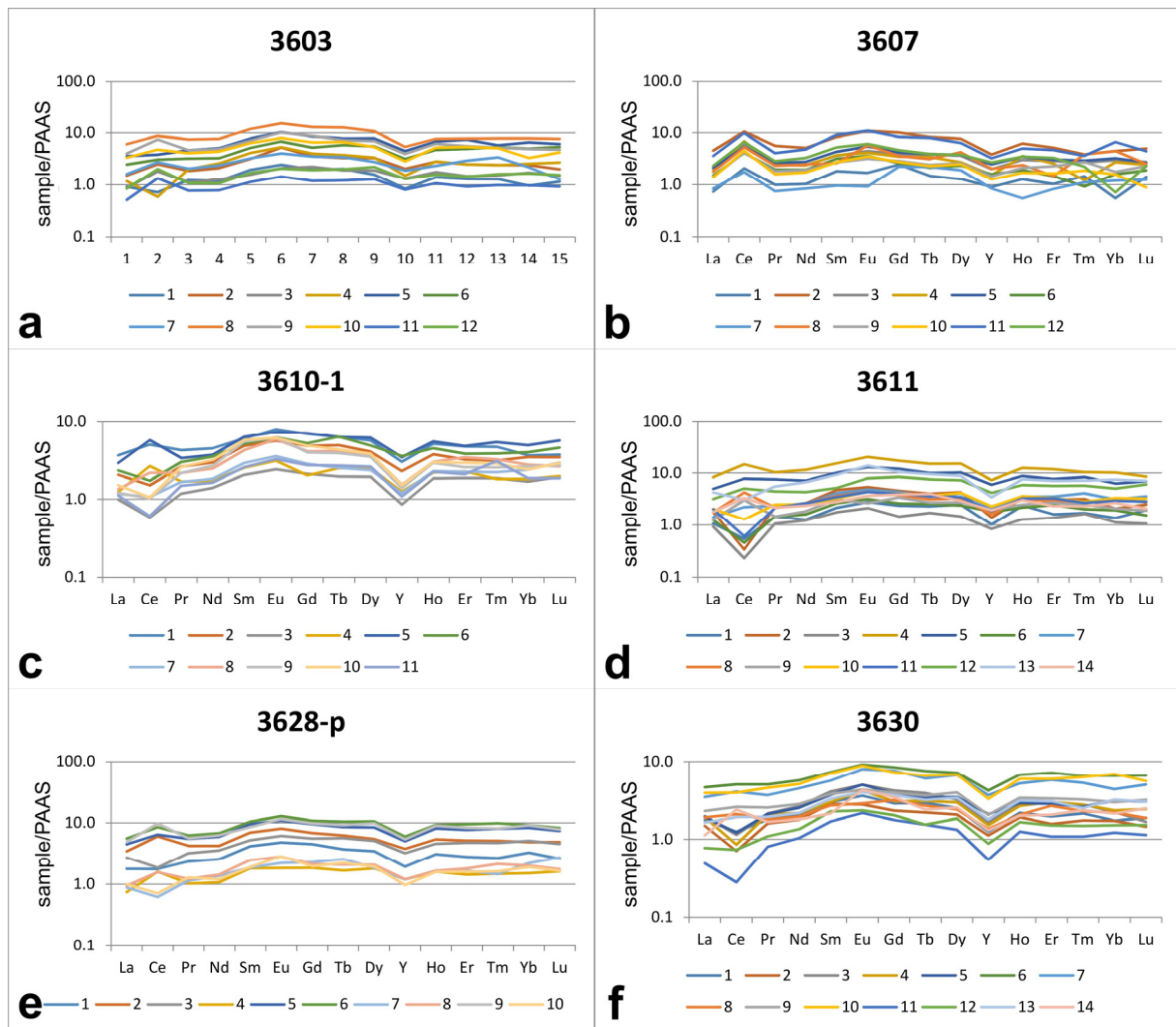
Figure 11. PAAS-normalized (after [31]) REE patterns of in situ analyses of nodules: (**a**) 3603; (**b**) 3607; (**c**) 3610-1; (**d**) 3611; (**e**) 3628-p; (**f**) 3630. Numbers are sample stations.

4.2.4. Correlations

In bulk nodule samples, Mn has a positive correlation (Table S3) with Sn, Sb (strong: correlation coefficient (CC) = 0.7–1), Li, Ni, Zn, Mo (moderate: CC = 0.5–0.7), V, Cu, Pb, Cd, Tl, and Ba (weak: CC = 0.3–0.5), and a negative correlation with Si, Al, Fe (strong), Na (moderate), K, Sc, Co, Ge, Zr, and Hf (weak). Iron has a positive correlation with Co, Hf (strong), Si, Na, P, As, Zr, Nb, W, Pb (moderate), Al, Mg, Ti, B, Ga, In, Ce, and U (weak), and a negative correlation with Mn, Sb (strong), Li, Zn, Cd, Sn (moderate), Ni, Cu, Mo, Ba, and Tl (weak). A positive correlation is observed between the following: Ti and REE, P, As, Sr, Y, Zr, Nb, In, Hf, Pb, Bi, Ca, Th, and U; P and REE, Ti, As, Sr, Y, Zr, Nb, Hf, Pb, U, Fe, Ca, Na, Y, Co, In, Bi, and Th; Y and REE, Ti, Sr, Zr, Nb, Hf, Bi, Th, U, Al, Mg, Na, P, Sc, Ni, Ga, Tl, and Pb; Co and Fe, As, Te, W, Pb, Si, P, Al, Zr, Nb, and Hf; Ni and Cu, Mo, Tl, Ti, Mn, Ca, V, Sr, Y, Sb, REE (without Ce), Bi, and Th; Cu and Li, Sb, Tl, Mn, Ni, Zn, Mo, and Pd; and REE and Ti, P, Ga, Sr, Y, Zr, Nb, Bi, Th, and U.

In the nodule layers, Mn has a positive correlation (Table S4) with Cu, Cd, Tl (strong), Mg, Na, Ni, Zn, Mo, Sb, Ba (moderate), Ca, K, Li, V, Ga, Sr, and W (weak), and a negative correlation with Si, Fe, Sc, Zr, and Hf. Iron has a positive correlation with P, As, Zr, Ce (strong), Si, Ti, Sc, Y, REE (without Ce), Hf, Pb, Bi, Th, U (moderate), Co, Sr, and Nb (weak), and a negative correlation with Mn, Ni, Cu, Zn, Mo, Cd, Sb, and Tl. A positive correlation is observed between the following: Ti and REE, P, Co, As, Sr, Y, Zr, Nb, Hf, Pb, Bi, Th, and U; P and Ca, REE, Co, As, Sr, Y, Zr, Nb, Hf, Pb, Bi, Th, and U; Y and Ca, P, REE, As, Sr, Zr, Pb, Bi, Th, and U; Ni/Cu and Mn, Mg, Na, Zn, Ga, Mo, Cd, Sb, and Tl; Ba and V, Mn, Mg, K, Sr, W, and Tl.

5. Discussion

5.1. Nodule Genetic Types

Classifications of the polymetallic nodules from the eastern part of the CCZ are based on morphology, size, surface texture, and growth environment. Morphological nodule types are discoidal, ellipsoidal, spheroidal, tabular, poly-nucleic, irregular, and fragments. Genetic classifications include three main types: hydrogenetic (H), diagenetic (D), and mixed hydrogenetic–diagenetic (HD) [11–13]. Hydrogenetic nodules are smaller (<4 cm), with Mn/Fe ratios < 3, low Ni and Cu content, and are enriched in Fe and Co. The mixed type nodules are 4–8 cm in size, with Mn/Fe ratios of 3–5. The diagenetic nodules are larger (>6 cm), with Mn/Fe ratios > 5, and enriched in Mn, Cu, and Ni. The D-type nodules can be clearly subdivided into two sub-types based on their Mn content and the Ni/Cu ratio. As a rule, contents of Mn, Ni, and Cu for D-type are $30 \pm 1\%$, $1.4 \pm 0.1\%$, and $1.2 \pm 0.1\%$, respectively. In type D1, contents of Mn reach 33% and Cu content is higher than that of Ni [33].

Based on their morphological characteristics, the studied nodules are classified on board according to [13] as diagenetic (3600, 3607, 3609-1, 3630), hydrogenetic–diagenetic (3603, 3604, 3610-1, 3611, 3512, 3621, 3628-p, 3629), and hydrogenetic (3615, 3623-p). The Mn/Fe ratio between 2.74 and 10.12 indicates that they are the hydrogenetic–diagenetic and diagenetic types, and only one (3607) is hydrogenetic [11,13]. Two nodules (3603 and 3610-1) have characteristic features of diagenetic D1 nodule types, where Mn > 33%, and Cu content is higher than that of Ni [33].

Other classification diagrams are also controversial, e.g., on the ternary Fe–Mn–(Co + Ni + Cu) × 10 diagram [34], as bulk nodules fall in or close to the hydrogenetic field while most of the in situ nodule analyses plot between the hydrogenetic and the diagenetic fields (Figure 12a). If we apply the ternary (Cu + Ni) × 15 − (Mn + Fe)/4 − (Zr + Ce + Y) × 100 diagram [35], bulk nodules fall in or close to the diagenetic field while most of the in situ nodule analyses plot close to the diagenetic field, and some of them plot in the hydrogenetic field (Figure 12b). REE criteria for discrimination of polymetallic nodules suggested by Bau et al. [36] determine most of the studied nodules as hydrogenetic (Ce/Ce* > 1, Y/Y* < 1, Nd > 100 ppm) although on the Ce/Ce*–Nd and Ce/Ce*–Y/Ho diagrams, they plot between the hydrogenetic and diagenetic types (Figure 13). Using all these data, a conclusion about a complex geological setting and changing conditions of nodule generation can be inferred.
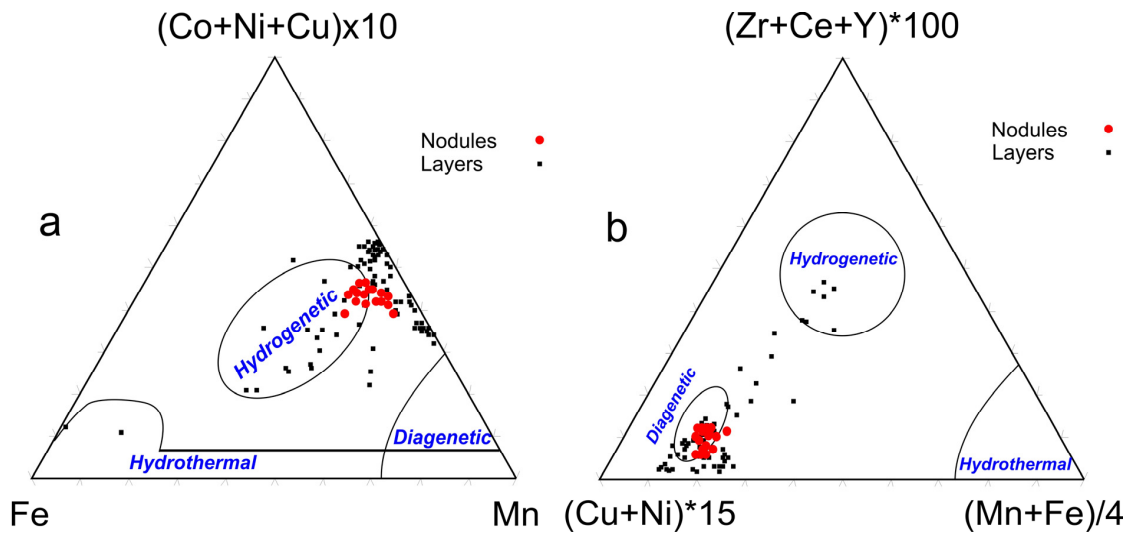
Figure 12. Comparison of bulk nodules and nodule layers on ternary Fe–Mn–(Co + Ni + Cu) × 10 diagram [34] (**a**) and (Cu + Ni) × 15 − (Mn + Fe)/4 − (Zr + Ce + Y) × 100 diagram [35] (**b**) for discrimination of polymetallic nodules and sediments.
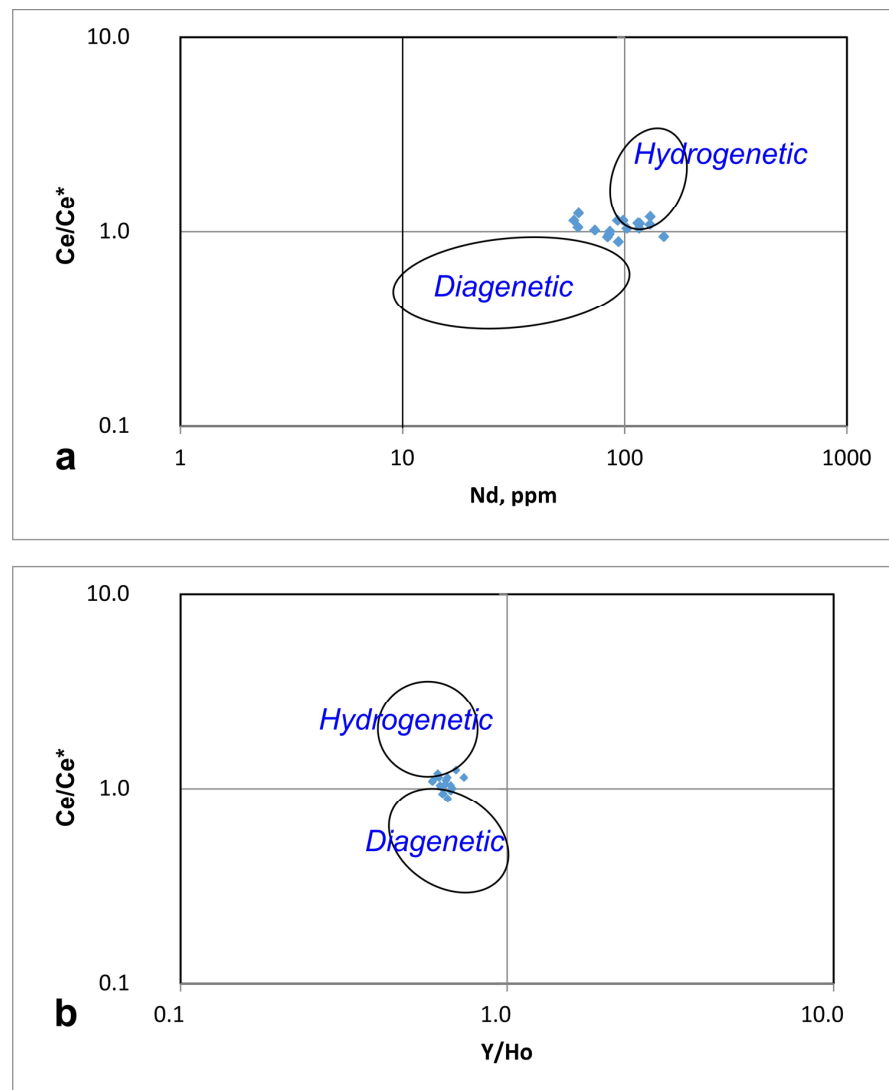

Figure 13. Ce/Ce*–Nd (**a**) and Ce/Ce*–Y/Ho (**b**) diagrams (after [36]) for discrimination of polymetallic nodules.

This conclusion is supported by data from the in situ EDS and LA-ICP-MS analyses. The nodule layers have variable mineral (todorokire or vernadite) and chemical compositions with a high or low Mn/Fe ratio. Most of them have Mn/Fe ratios > 10 and Ni + Cu between 2.5 and 5% and can be classified as diagenetic, while a small number with Mn/Fe ratio < 3 and Ni + Cu < 1.5% are hydrogenetic [11,20,37]. The different position of nodule layers found on the diagrams (Figure 12) of Bonatti et al. [34] and Josso et al. [35] probably reflect the periodically changing nodule growth mechanism and precipitation of the hydrogenetic or diagenetic layers [38].

The different styles of the nodules' growth during different periods of time is supported by the changing Ce anomalies registered in nodule layers. REEs are suggested to accumulate on Fe–Mn oxyhigroxide particles [39] and into authigenic apatite. The strong positive correlation of REE with Fe and P and negative correlation with Mn in our samples confirm Dubinin's suggestion. Negative Ce anomalies, together with LREE depletion relative to HREE, are characteristic of hydrothermal and diagenetic iron hydroxides, whereas positive Ce anomalies and LREE enrichment are typical for hydrogenetic pelagic nodules [39–42]. Our PAAS-normalized bulk analyses reveal no or weak positive Ce anomaly and fall between the hydrogenetic and diagenetic end members [43], which suggests a mixed hydrogenetic–diagenetic origin. Both chondrite- and PAAS-normalized REE patterns of the in situ nodule analyses show variable Ce anomalies between nodule layers. These variations in Ce anomalies correlate negatively with the Mn/Fe ratios and changes in layer genetic types (diagenetic or hydrogenetic). The change in Ce anomalies is a proof of a changing oxic/suboxic environment and is a useful and more exact indicator for the nodule layers' growth mechanisms [39,42].

All these different assessments of the nodule genetic types suggest periodical changes in diagenetic and hydrogenetic nodule growth in this part of the CCZ. Growth processes in the eastern part of the CCZ deposit might have been induced by the Plio-Pleistocene changes in the paleooceanographic conditions related to the deglaciation of the Northern Hemisphere [20] and the influence of Antarctic Bottom Water (AABW) flow that led to increased ventilation of the deep-ocean [44,45].

5.2. Behaviour of Elements in Pore Waters, Sediments, and Nodules

The bottom sediments and pore waters form the real environment for nodule formation. The environment is a result of sedimentation rate, bioturbation, oxidation conditions, certain bottom current conditions [13], and diagenetic process (biogeochemistry, adsorption, desorption, transformation, and migration) [13,42,46].

The comparison of the geochemical characteristics of previously reported data of pore waters and sediments [14–16] and polymetallic nodules (this study) from the six stations of the IOM exploration area provide evidence on the possible sources and processes of element concentration in the studied matrices. Table 2 shows the positive and negative correlations of Mn and Fe with other elements in the pore waters, bottom sediments, polymetallic nodules, and nodule layers. Copper is the only element which has positive correlation with Mn in all studied matrices of the deep-ocean floor environment. Five elements—Ni, Zn, Mo, Sb, and Ba—have positive correlations with Mn in sediments, bulk nodules, and nodule layers. Other elements correlate either positively (Cd, W, and Tl) or negatively (Si, Zr, Hf, and Pb) with Mn in two matrices. Manganese has variable (+/−) correlations with Fe, Co, and Na in different matrices. Iron has positive correlations with Ti, P, Zr, Nb, and Pb in sediments, nodules, and nodule layers and with REE, Y, and Th in sediments and nodule layers.

Table 2. Correlations of Mn and Fe in pore waters, sediments, bulk nodules, and nodule layers. Abbreviations: corr—correlation (positive (+)/negative (−)); **Al** (**bold**)—strong (0.7–1) correlation; *Co (Italic)*—moderate (0.5–0.69) correlation; Sr (normal)—weak (0.3–0.49) correlation; Cu—correlation in all matrices; Ni—correlation in 3 matrices. Data of pore waters and sediments are from [14–16].

Matrix	Pore Waters		Sediments		Bulk Nodules		Nodule Layers	
corr	+	−	+	−	+	−	+	−
Mn	**Al**, **Fe**, *Co*, *Y*, Cu		**Co**, **Ni**, **Cu**, *Zn*, *Mo*, *W*, Na, Sr Sb, Ba	*Ti*, *Pb*, Al, Fe K	**Sn**, **Sb**, *Li*, *Ni*, *Zn*, *Mo*, Cu, V, Cd, Ba Tl	**Si**, **Al**, **Fe**, *Na*, *K*, Sc, Co, Ge, Rb, Zr, Hf, Pb, U	**Cu**, **Cd**, **Tl** *Mg*, *Na*, *Ni*, *Zn*, *Mo*, *Sb*, *Ba*, Li, Ca, K, V, Sr, W	*Fe*, Si, Sc, Zr, Hf
Fe	**Al** **Mn** *Ba*		**Al**, **Ti**, **Ca**, **K**, **Mg** *P*, *Y*, *REE*, Ga, Zr Nb, Pb, Th	*Si*, *Ni*, *As*, *Mo*, *W* Mn	**Co**, **Hf**, *Si*, *Na*, *P*, *As*, *Zr*, *Nb Pb*, *W* Al, Mg, Ti, B, Ga, In, Ce, U	**Mn**, **Sb**, *Li*, *Zn*, *Cd*, *Sn* Ni, Cu Mo, Ba, Tl	**P**, **As**, **Zr**, **Ce**, *Si*, *Ti*, Sc, Y, REE, Hf, Pb, Bi, U, Th, Co, Sr, Nb	*Mn*, Li, Ni, Cu, Zn, Mo, Cd, Sb, Tl

In the pore water, Mn and Fe have highest concentrations in the geochemically active layer [15]. The pore waters accumulate metals from the oxidation of organic matter in deep-ocean sediments, which results in the reduction and dissolution of Mn oxides and associated elements (Ni, Cu, Li) [38]. Due to concentration gradients in the sediment, these metals diffuse upward and, on contact with oxygen-rich ocean water, are reoxidized and precipitate as 7A and 10A Mn oxides (disordered phyllomanganates) [7,38]. Manganese has a positive correlation with Fe (and Co) in pore waters but the correlation becomes negative in the sediments and nodules. Hence, Mn precipitates faster than Fe in the sediments and especially in nodules. In general, the Fe oxide-hydroxide (FeOOH-xH20, goethite or amorphous Fe oxide) precipitates first, which forms a surface particularly conducive to Mn oxide precipitation. Once in place, the Mn oxide surface is itself autocatalytic and effective in attracting subsequent Mn into the growth structure. It has a high adsorption capacity and is highly effective in attracting and sequestering other transition metals such as Ni and Cu [47,48]. That is why the nodules are enriched in Mn, Ni, and Cu in comparison to the host sediments. This trend can be illustrated on the Bonatti et al. [34] ternary diagram Fe–Mn–(Co + Ni + Cu) × 10 (Figure 14). The concentration of metals in pore water depends on the accumulation rate of the sediments and the processes of dissolution, reduction, and oxidation. In sediments and nodules, the deposition of metals depends on the presence of nuclei (fragments of old nodules, sediment material, volcanoclastic rocks, bioclastic material), well-oxygenated bottom waters, a semi-liquid surface layer, and bioturbation [13].

REE content in pore waters [15] is at least two orders of magnitude higher than in oceanic water [49] with moderate and heavy REE enrichment (Figure 15). The host sediments [14] have three orders of magnitude higher REE contents than the pore waters and comparatively flat patterns. The REE contents measured in the nodules are 2–3 times more elevated than in the host sediments and are 2–3 times higher in the richest nodule layers than in the bulk nodules. Figure 15 illustrates the trend of REE gradual enrichment from oceanic water trough pore waters and sediments to polymetallic nodules.

The decomposition and adsorption of organic matter and oxidation conditions are considered the main factors for the fractionation of REE in pore water [15]. REE enrichment in the deep-sea sediments is explained as the result of the interaction of several factors: low sedimentation rate, the presence of phosphate component near the seawater/sediment interface, high REE of the bottom seawater, oxidation conditions, certain bottom current conditions, and strong adsorption capacity of sediments [50–52]. In general, it was accepted that the REEs accumulate on Fe–Mn oxyhydroxide particles [39,53] and incorporate into authigenic apatite [51,52,54,55]. Our data on the concentrations and spatial distribution of the major and trace elements in the nodule layers (see Table S2) are in good agreement and in

support of the above conclusions. Negative Ce anomalies are characteristic for diagenetic Fe hydroxides, whereas a positive Ce anomaly is typical for hydrogenetic nodules [39,41,42,56]. The absence or weak positive Ce anomaly suggests a mixed hydrogenetic–diagenetic nodule type. The varying Ce anomalies in the nodules' layers suggest changing oxic/suboxic conditions. The Ce anomaly correlates with the Mn/Fe ratio and the genetic type (diagenetic or hydrogenetic) and could be a useful indicator for the nodule growth mechanisms [42].
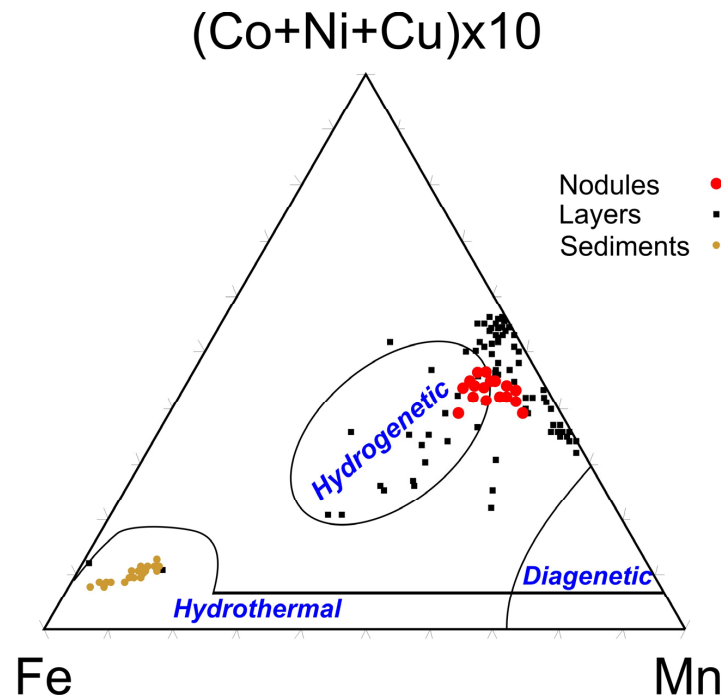

Figure 14. Comparison of sediments, bulk nodules, and nodule layers on ternary Fe–Mn–(Co + Ni + Cu) × 10 diagram [34] for discrimination of polymetallic nodules and sediments. Data of sediments are from [14].
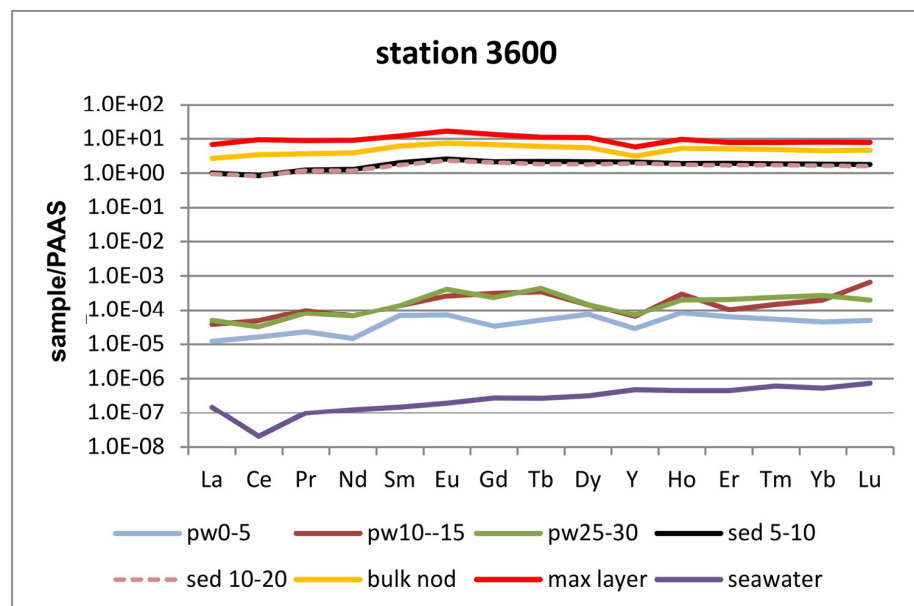

Figure 15. PAAS-normalized (after [32]) REE patterns of pore water layers (pw 0–5, pw 10–15, pw 25–30) [15], sediment layers (sed 5–10, sed 10–20) [14], bulk nodules (bulk nod), and richest nodule layers (max layer) of station 3600 compared to average deep oceanic water (seawater) [49].

5.3. REE and Critical Metal Enrichment Mechanisms

The application of a selective sequential leaching procedure applied by Koschinsky and Halbach [57] allowed for a separated dissolution of the major mineral phases of the studied polymetallic nodules and sediments and determination of the associated elements with special attention on the REE [58,59]. The bulk samples were selectively separated into four fractions of different phase solubilities showing different element mobilities and bonding forms. The results showed extraction of Mn in leach 2 in both nodules and sediments [58,59]. Cobalt, Ni, Cu, and Zn revealed similar behaviour due to the sorption of these elements onto MnO_2 phases [11,38]. Manganese has a high adsorption capacity of its oxides for cationic species, especially Ni^{2+}, Co^{3+}, and Cu^{2+}; the hydrated todorokite structure could be stabilized by the addition of Ni, Cu, Zn, and other divalent transition metals, leading to enhanced incorporation of these metals [47,48,60].

REE shows fractionation being partially extracted in leach 2 from 14 to 21% for HREE to 40–56% for La and Eu [58]. The extraction of Fe principally in leach 3 for the nodules is accompanied with a high level of P, REE, Zr, Nb, Mo, Sb, W, Pb, Bi, and U extraction [58,59]. Partial extraction of Fe in leach 2 attests that part of Fe is in the form of FeOOH intergrown with Mn oxide in vernadite, as was suggested by [57]. The extraction of P from sediments in leach 2 and the positive correlation of Mn and P could be a result of an authigenic fine-grained apatite which is intergrown with Mn oxyhydroxides. Huang and Fu [61] summarize the enrichment pathways as follows: (1) Ni, Cu, Zn, and Li enrichment through direct complexations on the Mn oxides; (2) Co, Ce, and Tl enrichment mainly through oxidation–substitution on the Mn oxides; (3) REY (except for Ce), Cd, Mo, W, and V partitioning between Fe and Mn (oxy)hydroxides through electro-attractiveness and overcoming repulsions.

High extraction of Fe, K, Ti, Rb, V, Zn, Zr, Nb, Mo, Sb, W, Ba, and U was registered in the sediment residual fraction [59]. This is related to detrital mineral phases like, illite, kaolinite, chlorite, andesine, zircon, rutile, and authigenic barite [49], as well as the influence of volcanic activity and/or hydrothermal processes [62]. Part of these elements (Zr, Nb, Mo, U) as well as Sc, Y, and REE have a strong positive correlation with P and form the third group of elements bound in the authigenic apatite [49,63]. The strong positive P–REE correlation suggests that the phosphate component is a main important carrier of REE in both nodules and sediments but Fe-Mn oxyhydroxides and clay minerals cannot be excluded as carriers of REE [7,39,51,64,65].

The influencing factors of critical metal enrichments in crusts and nodules are mainly growth rates, water depth variations, electro-chemical speciation, post-depositional phosphatization, and the structures of Fe-Mn adsorbents [61]. The effects of these factors greatly influence critical metal enrichments and their geochemical behaviours during enrichments in Fe-Mn crusts and nodules.

5.4. Critical Elements in Nodules

Previous research conducted in the IOM exploration area and its first generation minable blocks led to the determination of mineral resource estimate of wet polymetallic nodules [9,17]. Our results of bulk nodule samples confirmed the IOM data for Mn, Cu, Ni, Co, and Zn [17]. Furthermore, data on the significant presence of REE and other trace elements (Li, V, As, Y, Mo, Pd, Cd, Sb, W, Tl, and Pb) in the polymetallic nodules were obtained. The contents of Li, V, As, Mo, Tl, and W are slightly higher than those given for Fe-Mn nodules from CCZ [38]. Most of these elements are defined as critical raw materials [1]. At the same time, CCZ nodules are shown to contain a greater tonnage of Mn, Ni, Co, Tl, Y, and As than the entire global terrestrial reserve base [38]. The REE content in the studied nodules is lower than that given for the Fe-Mn nodules [49] and for other parts

of CCZ [63] but is nearly the same as that given for CCZ [42] and for the IOM exploration area [66,67]. The trace element contents of the studied nodules from the IOM exploration area in CCZ are similar with those of polymetallic nodule fields in Central Indian Ocean Basin with high Mn, Ni, and Cu, and moderate Co, Mo, and Li contents, which represent mixed hydrogenetic–diagenetic nodules [38,48]. They differ significantly from nodules from the Peru Basin, characterized by high Mn and very high Ni and Li contents result of diagenetic processes [7], and from the Penrhyn Basin and Northwestern Pacific nodules with the highest Ti, Co, and REY content, which primarily form through hydrogenetic precipitation [68,69].

Grades of REE in the polymetallic nodules are generally lower than those for the land-based deposits, but in terms of tonnages, they are much greater [7]. Additionally, a relative amount of HREE in the marine deposits, which are of higher economic importance than LREE, is quite high when compared to the land ones: up to 26% of the total REEs [7,70]. The different REE contents are related to different genetic nodule types: hydrogenetic type—the highest; diagenetic type—the lowest grades. The geochemical analyses reveal REE fractionation in the marine deposits [70]: the δ-MnO_2-phase preferentially carries LREEs, whereas the Fe-oxyhydroxides contain more HREEs [71,72].

REE and other critical trace elements are potential by-products of major metal mining [70], as well as elements relevant to metallurgical processing [73]. They can significantly increase the economic importance of exploited polymetallic nodules in the future. This explains the growing importance of deep-sea polymetallic nodules as a potential source for the future supply of critical raw materials.

The mining of polymetallic nodules will have biological, physical, and chemical impacts on the ocean floor and overlying water column. It is very difficult to predict the possible impact of mining on the deep-ocean ecosystems. The potential impact of nodule mining on the benthic environment was investigated during a number of experiments, which provide some insights into the sensitivity and recovery times of abyssal nodule communities subjected to mining disturbance. Some of these studies have been shown not to have any or to have minor deleterious effects on the ocean floor environment. For example, the benthic impact experiment test [74] found that the physical and chemical properties of the disturbed sediments in a track made 26 years ago on the seafloor in nodule fields of the CCZ at 5000 m depth did not change significantly over time. Depth variations in the Mn content in the sediment in the track were similar to those in the surrounding undisturbed sediment, and the benthic fauna has completely recovered. However, further research needs to be conducted and measures taken to preserve the deep-sea environment and minimize the harmful impact of mining activities.

6. Conclusions

The assessments of the nodule genetic types suggest a periodical change in diagenetic and hydrogenetic nodule growth. This probably relates to the Plio-Pleistocene changes in the paleooceanographic conditions during deglaciation of the Northern Hemisphere and the influence of AABW flow that leads to increased ventilation of the deep-ocean.

The results of the joint study of bottom sediments, pore waters, and polymetallic nodules show a complexity of the processes that influence the formation of these deposits. The changing oxic/suboxic and anoxic conditions are well documented in the chemistry of the nodule layers. Probably the most important controlling factors are sedimentation rate, bioturbation, adsorption, desorption, and oxidation but also growth rates, water depth variations, electro-chemical speciation, post-depositional phosphatization, and the structures of the Fe-Mn adsorbents.

The polymetallic nodule deposits in the IOM contract area are estimated as economically reasonable for future mining for Ni, Cu, Co, and Mn resources, and also contain other metals of economic importance such as REE, Li, V, As, Y, Mo, Pd, Cd, Sb, W, Tl, and Pb. REE and other critical metals are potential by-products of major metal mining and can significantly increase the economic importance of exploited polymetallic nodules in the future with the necessary protection of deep-ocean ecosystems.

Supplementary Materials: The following supporting information can be downloaded at: https://www.mdpi.com/article/10.3390/min15020154/s1. Table S1: The chemical compositions of 17 bulk nodule samples from H22_NE block of the IOM exploration area in the eastern part of the CCZ, NE Pacific; Table S2: Chemical composition of selected in situ nodule analyses from H22_NE block of IOM exploration area. Manganese content is from SEM-EDS analyses; Table S3: Correlation matrix for chemical elements from 17 bulk nodule samples from H22_NE block of IOM exploration area in eastern part of CCZ, NE Pacific; Table S4: Correlation matrix for chemical elements from 212 in situ analyses of nodule layers from H22_NE block of IOM exploration area in eastern part of CCZ, NE Pacific.

References

1. *COM (2023) 160*; Regulation of the European Parliament and of the Council Establishing a Framework for Ensuring a Secure and Sustainable Supply of Critical Raw Materials and Amending Regulations (EU) 168/2013, (EU) 2018/858, 2018/1724 and (EU) 2019/1020. European Commission: Brussels, Belgium, 2023; p. 77.

2. European Commission, Directorate-General for Internal Market, Industry, Entrepreneurship and SMEs; Bobba, S.; Carrara, S.; Huisman, J.; Mathieux, F.; Pavel, C. *Critical Raw Materials for Strategic Technologies and Sectors in the EU: A Foresight Study*; Publications Office: Luxembourg, 2020. Available online: https://data.europa.eu/doi/10.2873/58081 (accessed on 20 November 2024).

3. Kato, Y.; Fujinaga, F.; Nakamura, K.; Takaya, Y.; Kitamura, K.; Ohta, J.; Toda, R.; Nakashima, T.; Iwamori, H. Deep-sea mud in the Pacific Ocean as a potential resource for rare-earth elements. *Nat. Geosci.* **2011**, *4*, 535–539. [CrossRef]

4. Yasukawa, K.; Ohta, J.; Mimuraa, K.; Tanaka, E.; Takaya, Y.; Usui, Y.; Fujinaga, K.; Machida, S.; Nozaki, T.; Iijimae, K.; et al. A new and prospective resource for scandium: Evidence from the geochemistry of deep-sea sediment in the western North Pacific Ocean. *Ore Geol. Rev.* **2018**, *120*, 260–267. [CrossRef]

5. Pak, S.J.; Seo, I.; Lee, K.Y.; Hyeong, K. Rare Earth Elements and Other Critical Metals in Deep Seabed Mineral Deposits: Composition and Implications for Resource Potential. *Minerals* **2019**, *9*, 3. [CrossRef]

6. Ren, J.; He, G.; Yang, Y.; Yu, M.; Deng, Y.; Pang, Y.; Zhao, B.; Yao, H. Ultraselective enrichment of trace elements in seawater by Co-rich ferromanganese nodules. *Glob. Planet. Chang.* **2024**, *239*, 104498. [CrossRef]

7. Hein, J.; Mitzell, K.; Koschinsky, A.; Conrad, T. Deep-ocean mineral deposits as a source of critical metals for high- and green-technology applications: Comparison with land-based resources. *Ore Geol. Rev.* **2013**, *51*, 1–14. [CrossRef]

8. Volkmann, S.E.; Kuhn, T.; Lehnen, F. A comprehensive approach for a techno-economic assessment of nodule mining in the deep sea. *Miner. Econ.* **2018**, *31*, 319–336. [CrossRef]

9. Abramowski, T.; Urbanek, M.; Baláž, P. Economic Assessment of Polymetallic Nodules Mining Project with Updates to Present Market Conditions. *Minerals* **2021**, *11*, 311. [CrossRef]

10. Stoyanova, V.; Hikov, A.; Stefanova, E.; Milakovska, Z.; Abramowski, T.; Peytcheva, I.; Chavdarova, S.; Stavrev, M. Deep-sea polymetallic nodules as opportunity for future supply with critical raw materials. *Rev. Bulg. Geol. Soc.* **2021**, *82*, 153–155. [CrossRef]

11. Halbach, P.; Scherhag, C.; Hebisch, U.; Marchig, V. Geochemical and mineralogical control of different genetic types of deep-sea nodules from the Pacific Ocean. *Miner. Depos.* **1981**, *16*, 59–84. [CrossRef]

12. Kotliński, R.A. Metallogenesis of the World's ocean against the background of oceanic crust evolution. *Pol. Geol. Inst. Warszawa* **1999**, *4*, 1–59.

13. Kotlinski, R.; Stoyanova, V. Nodule coverage, morphology and distribution in the Eastern CCZ. In *ISA, Technical Study No 6: Prospector's Guide for Polymetallic Nodule Deposits in the Clarion-Clipperton Fracture Zone*; International Seabed Authority: Kingston, Jamaica, 2010; pp. 34–42.

14. Hikov, A.; Milakovska, Z.; Stoyanova, V.; Stefanova, E.; Abramowski, T.; Chavdarova, S.; Stavrev, M. REE and trace elements distribution in the deep-sea sediments from the Interoceanmetal (IOM) polymetallic nodule exploration area in the Clarion-Clipperton fractures zone, NE Pacific. *Compt. Rend. Acad. Bulg. Sci.* **2022**, *75*, 1018–1027. [CrossRef]

15. Milakovska, Z.; Hikov, A.; Stoyanova, V.; Peytcheva, I.; Lyubomirova, V.; Abramowski, T. REY in pore waters of sediments hosting Fe-Mn nodules of the Interoceanmetal exploration area in the Clarion-Clipperton Fracture Zone, NE Pacific. *Geol. Balc.* **2022**, *51*, 27–35. [CrossRef]

16. Milakovska, Z.; Hikov, A.; Stoyanova, V.; Peytcheva, I.; Abramowski, T. Trace element characteristics of pore water from the deep-sea sediments of the Interoceanmetal exploration area in the Clarion-Clipperton Fracture Zone, NE Pacific. *Rev. Bulg. Geol. Soc.* **2023**, *84*, 129–132. [CrossRef]

17. Baláž, P. Results of the second phase of deep-sea polymetallic nodules geological survey in Interoceanmetal Joint Organization licence area (2016–2021). *Miner. Slovaca* **2022**, *54*, 95–118. [CrossRef]

18. Kotliński, R. Sediments in the eastern CCZ. In *ISA, Technical Study No 6: Prospector's Guide for Polymetallic Nodule Deposits in the Clarion-Clipperton Fracture Zone*; International Seabed Authority: Kingston, Jamaica, 2010; pp. 43–52. ISBN 978-976-95268-2-2.

19. Baláž, P. Results of the first phase of the deep-sea polymetallic nodules geological survey in the Interoceanmetal Joint Organization licence area (2001–2016). *Miner. Slovaca* **2021**, *53*, 3–36.

20. Skowronek, A.; Maciag, L.; Zawadzki, D.; Strzelecka, A.; Baláž, P.; Mianowicz, K.; Abramowski, T.; Koněcný, P.; Krawcewicz, A. Chemostratigraphic and Textural Indicators of Nucleation and Growth of Polymetallic Nodules from the Clarion-Clipperton Fracture Zone (IOM Claim Area). *Minerals* **2021**, *11*, 868. [CrossRef]

21. International Seabed Authority. Available online: https://www.isa.org.jm/maps/interoceanmetal-joint-organization (accessed on 23 August 2024).

22. *ISBA/19/LTC/8*; Recommendations for the Guidance of Contractors for the Assessment of the Possible Environmental Impacts Arising from Exploration for Marine Minerals in the Area. Issued by the Legal and Technical Commission 13-24713; International Seabed Authority: Kingston, Jamaica, 2013; p. 32. Available online: https://www.isa.org.jm/documents/isba19ltc8 (accessed on 15 July 2023).

23. Milakovska, Z.; Stoyanova, V.; Hikov, A.; Abramowski, T.; Stefanova, E.; Peytcheva, I.; Chavdarova, S.; Stavrev, M. Depositional setting of the deep-sea sediments from an area of high nodule occurrence in the Clarion-Clipperton Fractures Zone, NE Pacific. In Proceedings of the Goldschmidt Conference 2021, Lyon, France, 4–9 July 2021; Abstract 5983. [CrossRef]

24. Krumbein, W.C. Application of logarithmic moments to size-frequency distributions of sediments. *J. Sed. Petrol.* **1936**, *6*, 35–47. [CrossRef]

25. Lisitzin, A.P. *Sedimentation in the World Oceans*; SEPM Special Publication 17; Rodolfo, K., Ed.; Society of Economic Paleontologists and Mineralogists: Tulsa, OK, USA, 1972; p. 218.

26. Bostrom, K. The origin and fate of ferromanganese active ridge sediments. International Seabed Authority. *Stockh. Contrib. Geol.* **1973**, *27*, 149–243.

27. Guillong, M.; Meier, D.; Allan, M.; Heinrich, C.; Yardley, B. SILLS: A MATLAB-based program for the reduction oflaser ablation ICP-MS data of homogeneous materials and inclusions. In *Mineralogical Association of Canada, Short Course 40*; Sylvester, P., Ed.; Mineralogical Association of Canada: Vancouver, BC, Canada, 2008; pp. 328–333.

28. Post, J.E.; McKeown, D.A.; Heaney, P.J. Raman spectroscopy study of manganese oxides: Tunnel structures. *Am. Mineral.* **2020**, *105*, 1175–1190. [CrossRef]

29. Dreiseitl, I. About geotechnical properties of the deep seabed polymetallic nodules. In Proceedings of the 18th International Conference on Transport and Sedimentation of Solid Particles, Prague, Czech Republic, 11–15 September 2017; p. 8.

30. Sun, S.; McDonough, W. Chemical and isotopic systematics of oceanic basalts: Implications for mantle compozition and processes. *Geol. Soc. Lond. Spec. Publ.* **1989**, *42*, 313–345. [CrossRef]

31. McLennan, S.M. Rare earth elements in sedimentary rocks: Influence of provenance and sedimentary processes. *Rev. Mineral.* **1989**, *21*, 169–200.

32. Johnson, E.; Post, J. Water in the interlayer region of birnessite: Importance in cation exchange and structural stability. *Am. Mineral.* **2006**, *91*, 609–618. [CrossRef]

33. Kotliński, R.; Stoyanova, V. Buried and Surface Polymetallic Nodule Distribution in the Eastern Clarion-Clipperton Zone: Main distinctions and similarities. *Adv. Geosci.* **2007**, *9*, 67–74. [CrossRef]

34. Bonatti, E.; Kraemer, T.; Rydell, H. Classification and genesis of submarine ironmanganese deposits. In *Ferromanganese Deposits on the Ocean Floor*; Horn, D., Ed.; The US National Science Foundation: Washington, DC, USA, 1972; pp. 149–165.

35. Josso, P.; Pelleter, E.; Pourret, O.; Fouquet, Y.; Etoubleau, J.; Cheron, S.; Bollinger, C. A new discrimination scheme for oceanic ferromanganese deposits using high field strength and rare earth elements. *Ore Geol. Rev.* **2017**, *87*, 3–15. [CrossRef]

36. Bau, M.; Schmidt, K.; Koschinsky, A.; Hein, J.; Kuhn, T.; Usui, A. Discriminating between different genetic types of marine ferro-manganese crusts and nodules based on rare earth elements and yttrium. *Chem. Geol.* **2014**, *381*, 1–9. [CrossRef]

37. Wegorzewski, A.; Kuhn, T. The influence of suboxic diagenesis on the formation of manganese nodules in the Clarion Clipperton nodule belt of the Pacific Ocean. *Mar. Geol.* **2014**, *357*, 123–138. [CrossRef]

38. Hein, J.; Koschinsky, A.; Kuhn, T. Deep-ocean polymetallic nodules as a resource for critical materials. *Nat. Rev. Earth Environ.* **2020**, *1*, 158–169. [CrossRef]

39. Dubinin, A. Geochemistry of Rare Earth Elements in the ocean. *Lithol. Miner. Resour.* **2004**, *39*, 289–307. [CrossRef]

40. Elderfield, H.; Greaves, M. Negative cerium anomalies in the rare earth element patterns of oceanic ferromanganese nodules. *Earth Planet. Sci. Lett.* **1981**, *55*, 163–170. [CrossRef]

41. Kuhn, T.; Bau, M.; Blum, N.; Halbach, P. Origin of negative Ce anomalies in mixed hydrothermal–hydrogenetic Fe–Mn crusts from the Central Indian Ridge. *Earth Planet. Sci. Lett.* **1998**, *163*, 207–220. [CrossRef]

42. Hein, J.; Koschinsky, A. Deep-Ocean Ferromanganese Crusts and Nodules. In *Treatise on Geochemistry*, 2nd ed.; Elsevier: Amsterdam, The Netherlands, 2014; Volume 13, pp. 273–291. [CrossRef]

43. Kuhn, T.; Wegorzewski, A.; Rühlemann, C.; Vink, A. Composition, Formation, and Occurrence of Polymetallic Nodules. In *Deep-Sea Mining Resource Potential, Technical and Environmental Considerations*; Sharma, R., Ed.; Springer: Berlin/Heidelberg, Germany, 2017; pp. 23–64.

44. Glasby, G.P. Manganese deposition through geological time: Dominance of the Post-Eocene environment. *Ore Geol. Rev.* **1988**, *4*, 135–144. [CrossRef]

45. Demidova, T. The physical environmental in nodule provinces of the deep sea. In *Deep-Seabed Polymetallic Nodule Exploration: Development of Environmental Guidelines*; International Seabed Authority: Kingston, Jamaica, 1998; pp. 79–116.

46. Dutkiewicz, A.; Judge, A.; Müller, D. Environmental predictors of deep-sea polymetallic nodule occurrence in the global ocean. *Geology* **2020**, *48*, 293–297. [CrossRef]

47. Morgan, C.L. Resource Estimates of the Clarion-Clipperton Manganese Nodule Deposits. In *Handbook of Marine Mineral Deposits*; Cronan, D.S., Ed.; CRC Press: Boca Raton, FL, USA, 2000; pp. 145–170.

48. Glasby, G.P. Manganese: Predominant Role of Nodules and Crusts. In *Marine Geochemistry, 2nd Revised, Updated and Extended Edition*; Schulz, H., Zabel, M., Eds.; Springer: New York, NY, USA, 2006; pp. 371–428.

49. Li, Y.-H.; Schoonmaker, J.E. Chemical Composition and Mineralogy of Marine Sediments. In *Treatise on Geochemistry*, 2nd ed.; Elsevier: Amsterdam, The Netherlands, 2014; Volume 9, pp. 1–35. [CrossRef]

50. Deng, Y.; Ren, J.; Guo, Q.; Cao, J.; Wang, H.; Liu, C. Rare earth element geochemistry characteristics of seawater and porewater from deep sea in western Pacific. *Sci. Rep.* **2017**, *7*, 16539. [CrossRef] [PubMed]

51. Ren, J.; Liu, Y.; Wang, F.; He, G.; Deng, X.; Wei, Z.; Yao, H. Mechanism and Influencing Factors of REY Enrichment in Deep-Sea Sediments. *Minerals* **2021**, *11*, 196. [CrossRef]

52. Ren, J.; Jiang, X.; He, G.; Wang, F.; Yang, T.; Luo, S.; Deng, Y.; Zhou, J.; Deng, X.; Yao, H.; et al. Enrichment and sources of REY in phosphate fractions: Constraints from the leaching of REY-rich deep-sea sediments. *Geochim. Cosmochim. Acta* **2022**, *335*, 155–168. [CrossRef]

53. Bau, M.; Koschinsky, A. Oxidative scavenging of cerium on hydrous Fe oxide: Evidence from the distribution of rare earth elements and yttrium between Fe oxides and Mn oxides in hydrogenetic ferromanganese crusts. *Geochem. J.* **2009**, *43*, 37–47. [CrossRef]

54. Koeppenkastrop, D.; De Carlo, E.H. Sorption of rare-earth elements from seawater onto synthetic mineral particles: An experimental approach. *Chem. Geol.* **1992**, *95*, 251–263. [CrossRef]

55. Jiang, X.-D.; Sun, X.-M.; Chou, Y.-M.; Hein, J.R.; He, G.-W.; Fu, Y.; Li, D.-F.; Liao, J.-L.; Ren, J.-B. Geochemistry and origins of carbonate fluorapatite in seamount Fe-Mn crusts from the Pacific Ocean. *Mar. Geol.* **2020**, *423*, 106135. [CrossRef]

56. Surya Prakash, L.; Ray, D.; Paropkari, A.L.; Mudholkar, A.V.; Satyanarayanan, M.; Sreenivas, B.; Chandrasekharam, D.; Kota, D.; Kamesh Raju, K.A.; Kaisary, S.; et al. Distribution of REEs and yttrium among major geochemical phases of marine Fe–Mn-oxides: Comparative study between hydrogenous and hydrothermal deposits. *Chem. Geol.* **2012**, *312–313*, 127–137. [CrossRef]

57. Koschinsky, A.; Halbach, P. Sequential leaching of marine ferromanganese precipitates: Genetic implications. *Geochim. Cosmochim. Acta* **1995**, *59*, 5113–5132. [CrossRef]

58. Hikov, A.; Milakovska, Z.; Lyubomirova, V.; Lihareva, N. REE distribution in sequential leached phases from deep-sea polymetallic nodules and sediments. *Rev. Bulg. Geol. Soc.* **2023**, *84*, 105–108. [CrossRef]

59. Hikov, A.; Milakovska, Z.; Lyubomirova, V.; Lihareva, N. Critical elements in sequential leached phases from deep-sea polymetallic nodules and sediments. In Proceedings of the 24rd International Multidisciplinary Scientific GeoConference SGEM 2024, Albena, Bulgaria, 28 June–8 July 2024; pp. 37–44. [CrossRef]

60. Post, J.E. Manganese oxide minerals: Crystal structures and economic and environmental significance. *Proc. Natl. Acad. Sci. USA* **1999**, *96*, 3447–3454. [CrossRef] [PubMed]

61. Huang, S.; Fu, Y. Enrichment Characteristics and Mechanisms of Critical Metals in Marine Fe-Mn Crusts and Nodules: A Review. *Minerals* **2023**, *13*, 1532. [CrossRef]

62. Zawadzki, D.; Maciag, Ł.; Abramowski, T.; McCartney, K. Fractionation Trends and Variability of Rare Earth Elements and Selected Critical Metals in Pelagic Sediment from Abyssal Basin of NE Pacific (Clarion-Clipperton Fracture Zone). *Minerals* **2020**, *10*, 320. [CrossRef]

63. Menendez, A.; James, R.; Lichtschlag, A.; Connelly, D.; Peel, K. Controls on the chemical composition of ferromanganese nodules in the Clarion-Clipperton Fracture Zone, eastern equatorial Pacific. *Mar. Geol.* **2019**, *409*, 1–14. [CrossRef]

64. Sa, R.; Sun, X.; He, G.; Xu, L.; Pan, Q.; Liao, J.; Zhu, K.; Deng, X. Enrichment of rare earth elements in siliceous sediments under slow deposition: A case study of the central North Pacific. *Ore Geol. Rev.* **2018**, *94*, 12–23. [CrossRef]

65. Abbott, A.; Löhr, S.; Trethewy, M. Are Clay Minerals the Primary Control on the Oceanic Rare Earth Element Budget? *Front. Mar. Sci.* **2019**, *6*, 504. [CrossRef]

66. Dimitrova, D.; Milakovska, Z.; Peytcheva, I.; Stefanova, E.; Stoyanova, V.; Abramowski, T.; Waelle, M. Trace element and REY composition of polymetallic nodules from the Eastern Clarion–Clipperton Zone determined by in-situ LA-ICP-MC analyses. *Compt. Rend. Acad. Bulg. Sci.* **2014**, *67*, 267–274.

67. Kozlowska-Roman, A.; Mikulski, S. Chemical and morphological characterization of polymetallic (Mn-Fe) nodules from the Clarion-Clipperton Zone in the Pacific Ocean. *Geol. Q.* **2021**, *65*, 57. [CrossRef]

68. Hein, J.; Spinardi, F.; Okamoto, N.; Mizell, L.; Thorburnc, D.; Tawake, A. Critical metals in manganese nodules from the Cook Islands EEZ, abundances and distributions. *Ore Geol. Rev.* **2015**, *68*, 97–116. [CrossRef]

69. Ren, J.; He, G.; Deng, X.; Deng, X.; Yang, Y.; Yao, H.; Yang, S. Metallogenesis of Co-rich ferromanganese nodules in the northwestern Pacific: Selective enrichment of metallic elements from seawater. *Ore Geol. Rev.* **2022**, *143*, 104778. [CrossRef]

70. Halbach, P.; Jahn, A. Concentrations and metal potentials of REEs in marine polymetallic nodule and Co-rich crust deposits. In *Deep Sea Mining Value Chain: Organization, Technology, Development*; Abramowski, T., Ed.; Interoceanmetal Joint Organization: Szczecin, Poland, 2016; pp. 119–131.

71. Ohta, A.; Kawabe, I. REE(III) adsorption onto Mn dioxide (δ-MnO$_2$) and Fe oxyhydroxide: Ce(III) oxidation by δ-MnO$_2$. *Geochim. Cosmochim. Acta* **2001**, *65*, 695–703. [CrossRef]

72. Ren, Y.; Sun, X.; Guan, Y.; Xiao, Z.; Liu, Y.; Liao, J.; Guo, Z. Distribution of Rare Earth Elements plus Yttrium among Major Mineral Phases of Marine Fe-Mn Crusts from the South China Sea and Western Pacific Ocean: A Comparative Study. *Minerals* **2019**, *9*, 8. [CrossRef]

73. Mohwinkel, D.; Kleint, C.; Koschinsky, A. Phase associations and potential selective extraction methods for selected high- tech metals from ferromanganese nodules and crusts with siderophores. *Appl. Geochem.* **2014**, *43*, 13–21. [CrossRef]

74. Khripounoff, A.; Caprais, J.; Crassous, P.; Etoubleau, J. Geochemical and biological recovery of the disturbed seafloor in polymetallic nodule fields of the Clipperton-Clarion Fracture Zone (CCFZ) at 5,000-m depth. *Limnol. Oceanogr.* **2006**, *51*, 2033–2041. [CrossRef]